Study of Charge Recombination in Organic Solar Cells

Ji-Hyun Lee

The Graduate University for Advanced Studies, SOKENDAI

School of Physical Sciences

Dept. of Functional Molecular Science

Contents

Chapter 1: General Introduction

1.1 Background of Organic Solar Cells

1.1.1 History

Organic solar cells (OSCs) are the type of photovoltaic device that uses organic semiconductor materials. The first photovoltaic effect using organic semiconductor molecule was reported by Calvin in 1958 [1]. The active layer of the organic photovoltaic device was deposited using vacuum evaporation with single organic material of *p*-phenylenediamine and sandwiched electrode. The device showed low power conversion efficiency (PCE) as ~0.1% because of high internal cell resistance. Furthermore, quantum efficiency of the device with single organic material is low. Therefore, the maximum power output was 3×10^{-12} W, and the maximum photocurrent was only 1.5×10^{-8} mA. The breakthrough in photocurrent was suggested by Tang in 1986 [2]. Tang demonstrated two-layer organic photovoltaic cells using copper phthalocyanin and perylene tetracarboxylic derivative which the performance each short-circuit current density (J_{SC}): 2.3 mA cm^{-2}, open-circuit voltage (V_{OC}): 0.45 V, fill factor (FF): 0.65 V and PCE: 1% was reported. Furthermore, Hiramoto reported a tandem structure in 1990[3], and a blended junction cells of small-molecule was proposed in 1991 [4,5]. In 1992, Sariciftci reported a heterojunction cell using polymer (MEH-PPV) as a donor and C_{60} as an acceptor [6]. Furthermore, Yu proposed bulk polymer heterojunction cells by blending the semiconducting polymer with C_{60} in 1995 [7].

The development of organic semiconductor materials has improved the performance of OSCs. The low bandgap polymer was devised to harvest a wide range of absorption of

photons and increase the efficiency of the device [8–10]. Moreover, non-fullerene acceptors were provided for near-infrared absorption [11–13].

1.1.2 Device structure

The first OSCs had a single-layer structure in which a single organic substance was placed between two metal electrodes (**Figure 1.1.1 (a)**). Nowadays, the OSCs comprise an active layer, transparent electrode, metal electrode, and buffer layer. In general, indium tin oxide (ITO) is used as the transparent electrode. The most typical structure of OSCs is ITO/hole transporting layer/electron transporting layer/metal electrode. On the other hand, the structure of inverted OSCs is ITO/electron transporting layer/hole transporting layer/metal electrode. Because the work function is high, either Au or Ag are used for the metal electrode in the inverted structure.

Planar heterojunction (PHJ) OSCs that include donor and acceptor were reported by Tang [2]. Efficient exciton dissociation occurred by the D/A interface. Donor materials that were deposited on transparent electrodes act as a hole transporting layer, and acceptor materials that were deposited on the donor layer act as the electron transporting layer (**Figure 1.1.1 (b)**).

Except for the active layer, the composition of bulk heterojunction (BHJ) OSCs is similar to that of PHJ (**Figure 1.1.1 (c)**). In general, the active layer of BHJ is fabricated by the spin-coating of a mixed solution of donor and acceptor. The morphology of the active layer is strongly affected by the following conditions such as mixing ratio, concentration, organic solvent, additive, spin speed, and thermal annealing.

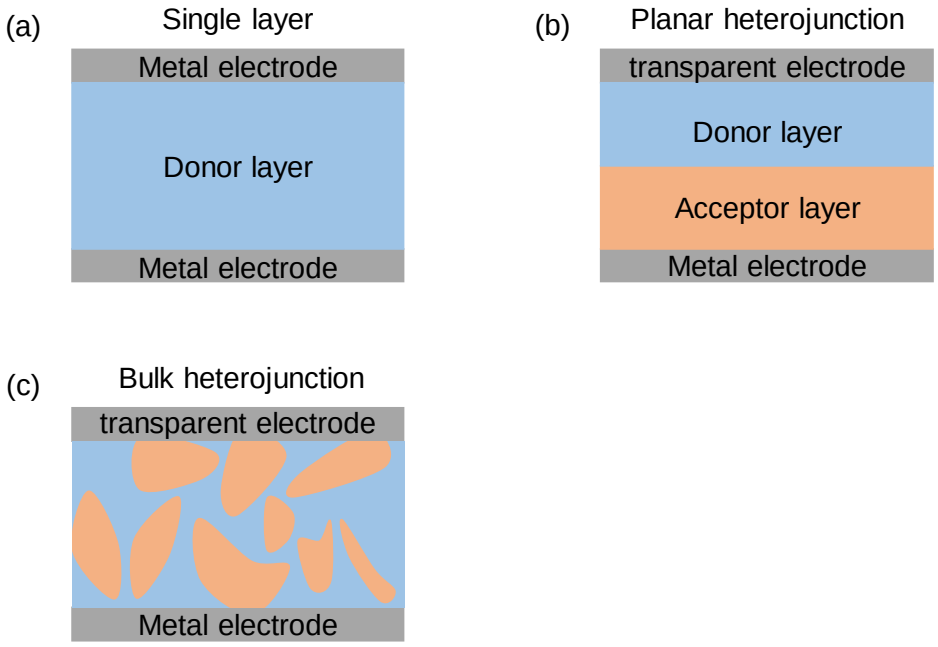

Figure 1.1.1 Schematic of organic solar cells (a) single layer, (b) planar heterojunction and (c) bulk heterojunction.

1.1.3 Fabrication method

The blended active layer in OSCs is prepared by the co-deposition technique or spin-coating. The thermal evaporation technique under high vacuum conditions is useful to fabricate the bilayer structure. The thickness of the layer can be controlled at the 10^{-10} m level precision using high vacuum deposition. The co-deposition technique is a method for simultaneously depositing two or more different substances. By simultaneously depositing a dopant and a host molecule, a *p*-type or *n*-type organic semiconductor thin film and organic *pn*-homojunction can be obtained [14–17]. Note that it is easy to control the concentration of the dopant and obtain the doped crystal because the deposition rate of each source can be separately controlled [18–20].

Spin-coating is a fabrication technique for a thin film on a flat substrate. The spin-coating technique is used in wet processes, and is particularly advantageous for fabricating blended structures [21]. The thickness of the film layer depends on spin speed, the solvent, and the concentration of the solution. In general, volatile solvents are applied.

1.2 Photoconversion mechanism

1.2.1 Excition generation and dissociation

Figure 1.2.1 shows a schematic of the photoconversion mechanism in bilayer organic solar cell contracted by a hole transporting layer (donor) and an electron transporting layer (acceptor). An exciton that is a photogenerated hole–electron pair is described as a simple hydrogen atom model, and the attractive force is determined by Coulomb's law [22]:

$$F = \left(\frac{1}{4\pi\varepsilon\varepsilon_0}\right)\left(\frac{q_1 q_2}{r^2}\right) \quad \text{equation 1.2.1}$$

where q_1 and q_2 are the elementary charges of the hole and electron, respectively, r is the distance between both, ε_0 is the vacuum permittivity, and ε is the relative permittivity of the solid. Each organic semiconductors has a small ε and a short exciton radius, therefore the hole and electron pair strongly attract. Note that the thermal energy at room temperature is insufficient to dissociate the exciton to free holes and electrons. Therefore, monolayer OSCs generate few photocurrents. After Tang's study, the D/A interface accelerated the exciton dissociation into free holes and electrons [2]. Thus, using donor and acceptor materials became the most useful and basic method in recent studies.

1.2.2 Charge transfer state formation

Charge transfer (CT) states are formed after Frankel-type exciton dissociating at the D/A interface. When excitons reach to D/A interface before decaying, the electrons transfer from the lowest unoccupied molecular orbital (LUMO) of the donor molecule to the LUMO of the acceptor molecule or the hole transfer to the highest occupied molecular

orbital of the donor molecule. Separated holes and electrons are localized at the D / A interface and stabilized by coulombic attraction[23,24].

1.2.3 Charge transfer state dissociation into free charge

The hole and electron charge pair of CT state is separated into free carriers. Both holes and electrons that have become free carriers are transported from one molecule to another molecule, and this transport is described as a hopping conduction. Certain holes and electrons attract and reform to the CT state at the D/A interface. This bypass process, primarily charge recombination, causes a photocurrent loss in OSCs.

1.2.4 Charge transport and collection

After dissociation, both hole and electron are transported to the electrode via the donor and acceptor using the potential difference termed as drift current or by the charge concentration difference as the diffusion current. Charge transport in OSCs is described by the hopping conduction model in which the charge is transported from one molecule to the adjacent molecule. At the electrode, free hole and electron are collected to anode and cathode, respectively. The ohmic contact without energy barrier at the organic semiconductor/electrode interface is important to collect charge carriers. For ohmic contact, sufficient amounts of high or low work function material is inserted between the organic semiconductor layer and electrode as the buffer layer.

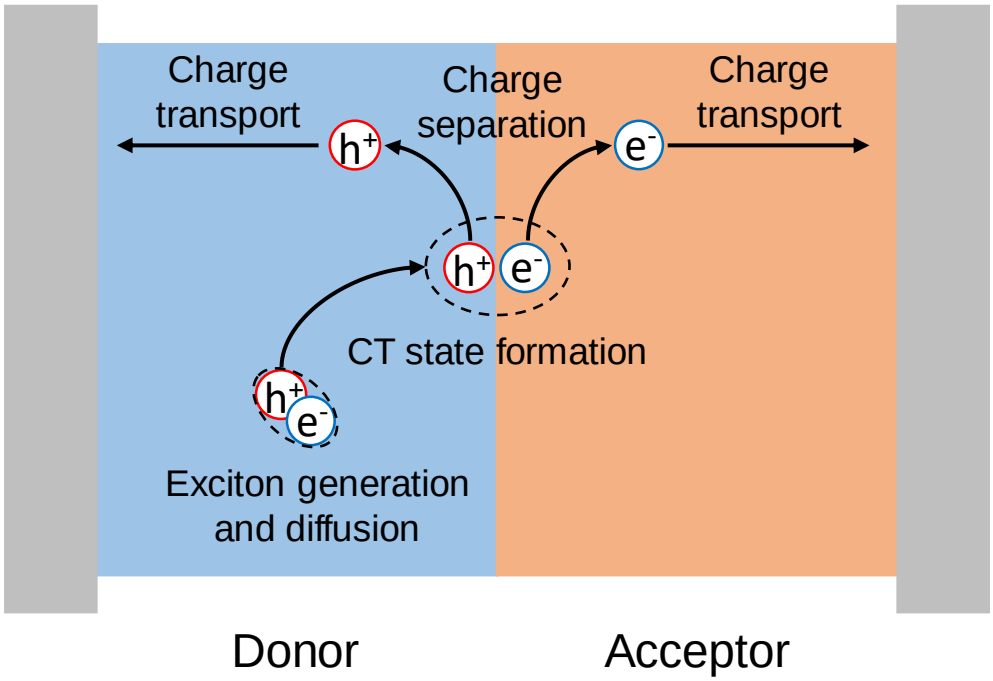

Figure 1.2.1 Schematic of photoconversion process in OSCs.

1.3 Charge recombination

1.3.1 Geminate and non-geminate recombination

Geminate recombination is one of the recombination processes that decay from the CT state to the ground state. In OSCs, the process of going from exciton to free carriers is strongly related to coulombic binding energy between photo-excited geminate hole-electron pairs. The coulombic binding energy must be overcome for the geminate pair to dissociate. Otherwise, the geminate recombination occurred. Using the energy difference between the optical bandgap and the CT state, free carriers are efficiently generated. In particular, the combination of polymer donor and fullerene acceptor shows efficient charge dissociation [25–28].

After dissociating the CT state, certain free electrons encounter holes at the D/A interface and recombine to the ground state. This non-geminate recombination is called "bimolecular recombination," which includes radiative recombination and non-radiative recombination. Bimolecular recombination is explained by Langevin recombination [29], which is the dominant recombination mechanism in a low-mobility material and a band-to-band recombination process. Furthermore, temperature is an important factor in bimolecular recombination. CT binding energy in organic materials is stronger than that in inorganic materials; therefore, CT state recombination is strongly affected by temperature[30]. Thus, bimolecular recombination increases with temperature. In addition, trap-assisted recombination is attributed to a trapped charge in the trap state within the bandgap[31,32]. In OSCs, CT state recombination is the primary problem of V_{OC} loss.

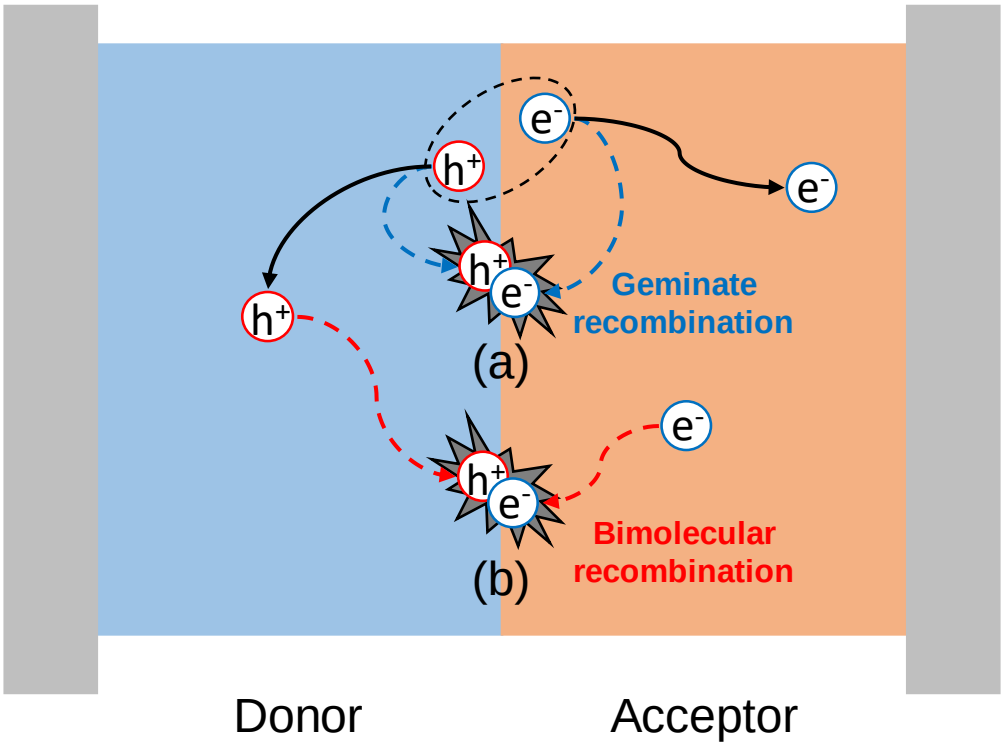

Figure 1.3.1 Schematic of recombination process in OSCs.

1.3.2 Radiative recombination and non-radiative recombination

Bimolecular recombination occurs because of light emission or thermal relaxation. The former is called radiative recombination, whereas the latter is called non-radiative recombination. **Figure 1.3.2** shows the schematic of radiative (blue) and non-radiative (brown) recombination. *j* and *i* are the vibration modes of the ground state and CT state, respectively. The vibrational coupling between both states easily induces non-radiative recombination. In the radiative recombination process, carriers directly transfer from the CT state to the ground state. Thus, light is emitted from the energy lost in the process.

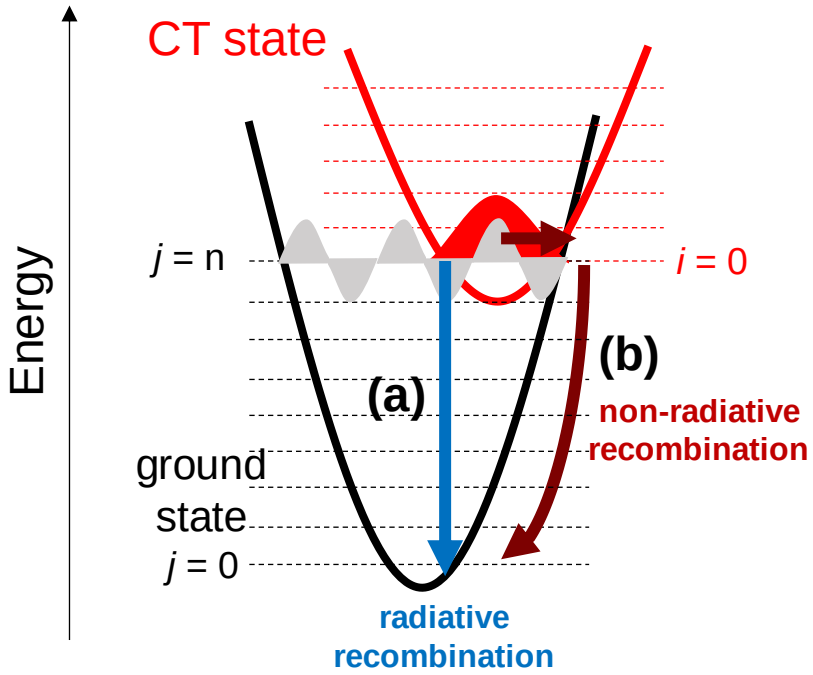

Figure 1.3.2 Schematic of the mechanism of the (a) radiative and (b) non-radiative recombination from the CT states to ground states.

1.4 Device performance

OSCs are evaluated by external quantum efficiency (EQE) and power conversion efficiency (PCE).

1.4.1 Quantum efficiency

EQE of OSCs is the ratio of the number of charge carriers collected to the number of photons irradiated from outside and estimated under monochromatic light irradiation; the equation is given by:

$$\mathrm{EQE} = \frac{n_{electron}}{n_{photon}} = \frac{(J_{\mathrm{SC}})\,(hc)}{(P_{in})\,(\lambda e)} \qquad \text{equation 1.4.1}$$

where J_{SC} is short-circuit current density, P_{in} is incidenct power density, $n_{electron}$ and n_{photon} are the number of electrons extracted from the OSC and irradiating photon to the OSC, respectively; h is Planck's constant; c is the speed of light; λ is the wavelength of irradiated light; and e is the elementary charge.

Internal quantum efficiency (IQE) is the ratio of the number of charge carriers collected to the number of photons absorbed by OSCs and the equation is given by

$$\mathrm{IQE} = \frac{n_{electron}}{n_{absorb}} = \frac{\mathrm{EQE}}{1-\mathrm{Reflection}-\mathrm{transmission}} \qquad \text{equation 1.4.2}$$

where n_{absrob} is the number of absorbed photons. The IQE is obtained by correcting EQE curve and measuring transmittance and reflectance of a device.

1.4.2 PCE evaluation of OSCs

Power conversion efficiency (PCE) is calculated from the *J–V* characteristic under simulated light irradiation. PCE of solar cells is sensitive to the wavelength and intensity of irradiated light, so it is measured under unified conditions. The standard condition for estimating current density-voltage (*J–V*) characteristic is air mass (A.M.) 1.5, and the spectrum of the light source is tuned to sunlight on the surface of the Earth by sunlight at an incident angle of 48.2°. In general, the light intensity is adjusted to 100 mW cm^{-2}. **Figure 1.4.1** shows a typical *J–V* curve. The dash line is measured under dark. This curve shows the characteristics of the diode. The equation of curve is explained by equivalent circuit model (section 1.4.5). The solid line is the *J-V* curve that is measured under standard light irradiation. The PCE is produced using three parameters: short-circuit current density (J_{SC}), open-circuit voltage (V_{OC}), and fill factor (FF). The equation is given by:

$$\mathrm{PCE} = \frac{J_{\mathrm{SC}} \times V_{\mathrm{OC}} \times \mathrm{FF}}{P_{\mathrm{in}}} \times 100 = \frac{J_{\mathrm{MAX}} \times V_{\mathrm{MAX}}}{P_{\mathrm{in}}} \times 100 \qquad \text{equation 1.4.3}$$

where P_{in} is the incident power density. Thus, FF is determined by the following equation:

$$\mathrm{FF} = \frac{J_{\mathrm{MAX}} \times V_{\mathrm{MAX}}}{J_{\mathrm{SC}} \times V_{\mathrm{OC}}} \qquad \text{equation 1.4.4}$$

Where J_{Max} and V_{Max} are the current density and voltage at maximum output power density, respectively.

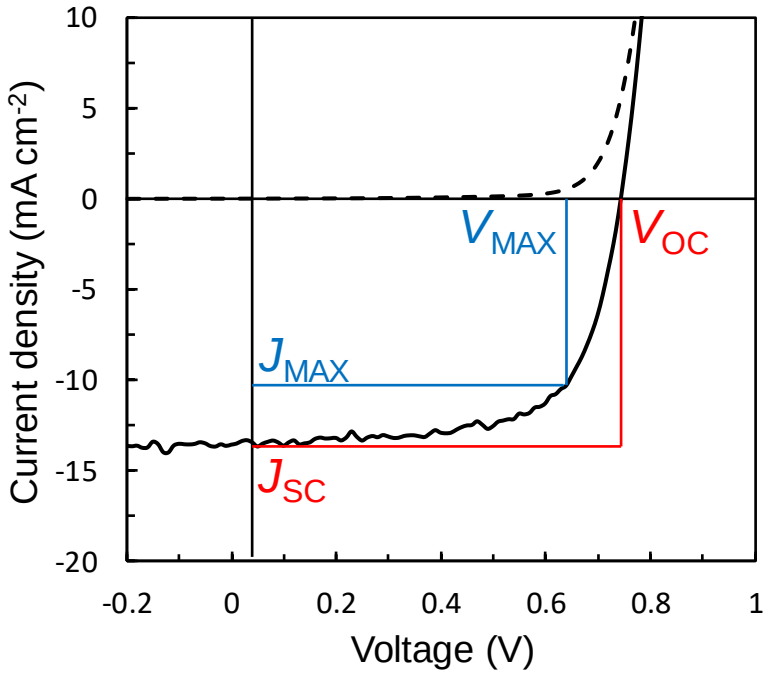

Figure 1.4.1 Typical *J*-*V* curve of OSCs.

1.4.3 Short-circuit current

Short-circuit current (I_{SC}) is the photocurrent from OSC when the applied voltage is 0 V. The short-circuit current density (J_{SC}) is the I_{SC} divided by the cell area.

$$J_{SC} = I_{SC}/A \quad \text{equation 1.4.5}$$

Under short-circuit condition that is under a large internal electric field, the energy loss process occurs during the charge separation and transport process. This indicates that the J_{SC} includes the information charge recombination. In particular, geminate recombination is a major loss process under short-circuit conditions [33].

1.4.4 Open-circuit voltage

Open-circuit voltage (V_{OC}) is the maximum voltage available from OSCs and can be reported at zero photocurrents. Experimentally, V_{OC} shows a linear dependence on the energy difference between the HOMO of the donor and the LUMO of an acceptor. Even with the same D/A combination, the V_{OC} shows different values because of structure or electrical interaction at the D/A interface. In general, the V_{OC} value is determined by the CT state energy and the voltage loss.

Furthermore, the temperature-related equation of V_{OC} is determined by the following:

$$V_{OC} = \frac{nkT}{e} \ln\left(\frac{J_{ph}}{J_0} - 1\right)$$

$$\approx \frac{nkT}{e} \ln\left(\frac{J_{ph}}{J_0}\right) \quad \text{equation 1.4.6}$$

where J_0 is the dark saturation current density, J_{ph} is the photocurrent density, n is the ideality factor, k is Boltzmann's constant, T is temperature and e is the elementary charge. The equation indicates that the V_{OC} linearly increases with temperature. However, because of temperature changes in carrier concentration, J_0 rapidly increases with temperature and is expressed using the Arrhenius equation,

$$J_0 = J_{00}\exp(-\frac{\varphi}{nkT}) \quad \text{equation 1.4.7}$$

where the pre-exponential term J_{00} is an electronic interaction term and φ is the activation energy. φ can be considered as CT state energy (E_{CT}) under open-circuit condition; therefore, the relational expression between E_{CT} and V_{OC} is reported as follows:

$$eV_{OC} = E_{CT} - nkTln(\frac{J_{00}}{J_{ph}}) \quad \text{equation 1.4.8}$$

This equation represents V_{OC} in one energetic term and the other recombination loss term. Thus, the most efficient methods to enhance V_{OC} are increasing E_{CT} and decreasing the recombination loss.

1.4.5 Equivalent circuit

The *J-V* curve of OSCs under light irradiated is given by equivalent circuit equation:

$$J = \frac{J_0}{1+{R_S}/{R_p}}\left\{\exp\left(\frac{q(V-R_SAJ)}{nk_BT}\right)-1\right\} + \frac{V-R_SAJ}{R_pA} - J_{ph} \quad \text{equation 1.4.9}$$

where J is the current density, V is the applied voltage, J_0 is the dark saturation current density, n is the ideality factor of the diode, R_S is series resistivity, R_P is shunt resistivity, A is cell area, k_B is Boltzmann's constant, T is temperature and J_{ph} is photocurrent

density[34]. J_{ph} is the photocurrent generation part that depends on the light intensity and applied voltage. Noted that J_{ph} is 0 under dark conditions. The first and second terms are represented using a diode. In particular, both J_0 and n are related to recombination. When 0 V is applied under dark conditions, the thermal activation and recombination current are balanced. Thus, J_0 reflects the recombination current density under zero bias conditions. As J_0 increases, the J–V curve shifts to the lower voltage side, resulting in lower V_{OC}. Thus, a small J_0 is desirable; the ideality factor n is dominated by band-to-band recombination. In OSCs, n increases because of trap-assisted recombination. The value of n is 1 under ideal conditions without trap-assisted recombination. In general, the value of n is between 1 and 2 in OSCs [35]. Both J_{SC} and FF are related to R_S; if R_S is large, J_{SC} and FF decrease. R_P is directly related to the leak current of the device. If R_P is small, V_{OC} and FF decrease; thus, small R_S and large R_P are desirable.

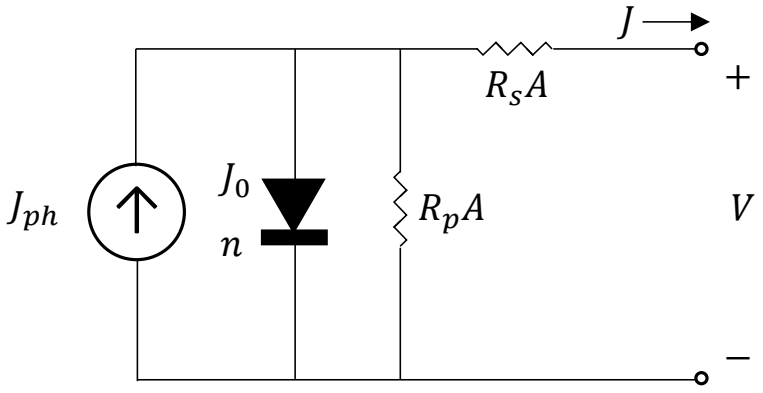

Figure 1.4.2 Equivalent circuit model for solar cells

1.4.6 Fill factor

The fill factor (FF) is an indicator of OSC quality and represented by the *J*–*V* curve, where it is the ratio of both rectangle areas of **Figure 1.4.1**; it is shown in Equation 1.4.4. In general, the FF of OSCs is in the range of 50%–70%, and even for the inorganic solar cells, the maximum FF is reported at 90%[34]. FF includes information on charge recombination, which shows the internal electric field dependence. In particular, bimolecular recombination is dominated in V_{OC} conditions. Moreover, both R_S and R_P of OSC are directly affected by FF, as explained in the Section 1.4.5.

1.5 Organic semiconductor materials

Organic semiconductor materials can influence OSC performance. For example, the HOMO–LUMO gap between donor and acceptor molecules is related to V_{OC}, and the carrier mobility affects the charge carrier transport and collection efficiency. Recently, for enhancing the PCE of OSCs, electron–donor and electron–acceptor organic semiconductors have been developed. In particular, organic semiconductors for BHJ require charge transport and tunable light absorption[36].

1.5.1 Donor

In OSCs, electron-donor materials donate electrons to another compound. Thus, a hole is produced from the lack of electron. First, phthalocyanine or merocyanine was used as small molecule organic semiconductors for the active layer (**Figure 1.5.1**) [37,38]. However, for efficient light absorption, polymers have been noticed and developed. Moreover, high hole mobility with wide absorption band molecules were reported. Thus, as an efficient low hand gap donor material, poly[(4,4-bis(2-ethylhexyl)-cyclopenta-[2,1-b;3,4-b`]dithiophene)-2,6-diyl-alt-2,1,3-benzothiadiazole-4,7-diyl] (PCPDTBT) has been proposed [39,40]. poly[4,8-bis[(2-ethylhexyl)oxy]benzo[1,2-b:4,5-b`]dithiophene-2,6-diyl][3-fluoro-2-[(2-ethylhexyl) carbonyl]thieno[3,4-b]thiophenediyl (PTB7) [41,42] and poly(3-hexylthiophene) P3HT[43,44] are well-studied materials.

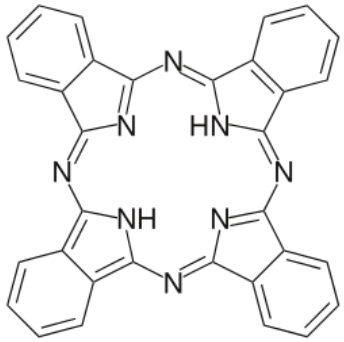

Phthalocyanine

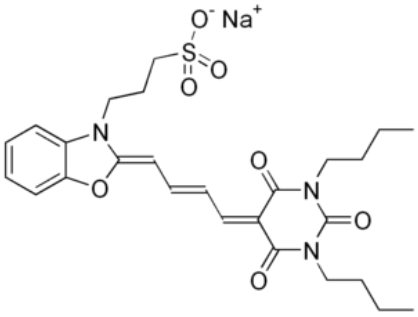

merocyanine

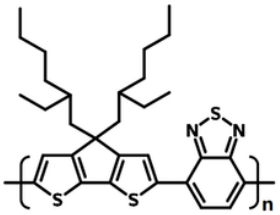

PCPDTBT

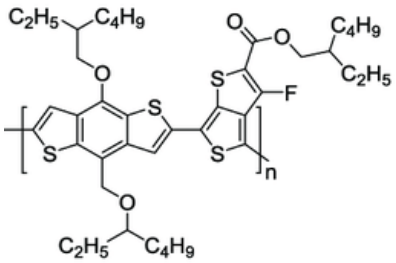

PTB7

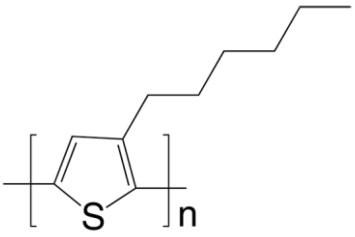

P3HT

Figure 1.5.1 Chemical structure of the donors

1.5.2 Acceptor

Electron acceptor materials accept electrons transferred from other materials. PCBM ([6,6]-phenyl-C61-butyric acid methyl) and its derivatives combine with polymer donors to form BHJ because electron transport is efficient; however, PCBM has poor light absorption. Therefore, non-fullerene acceptors are focused on their light absorption efficiency, e.g., OSCs using Y6 as an acceptor show high-efficiency PCE of >15%[45,46].

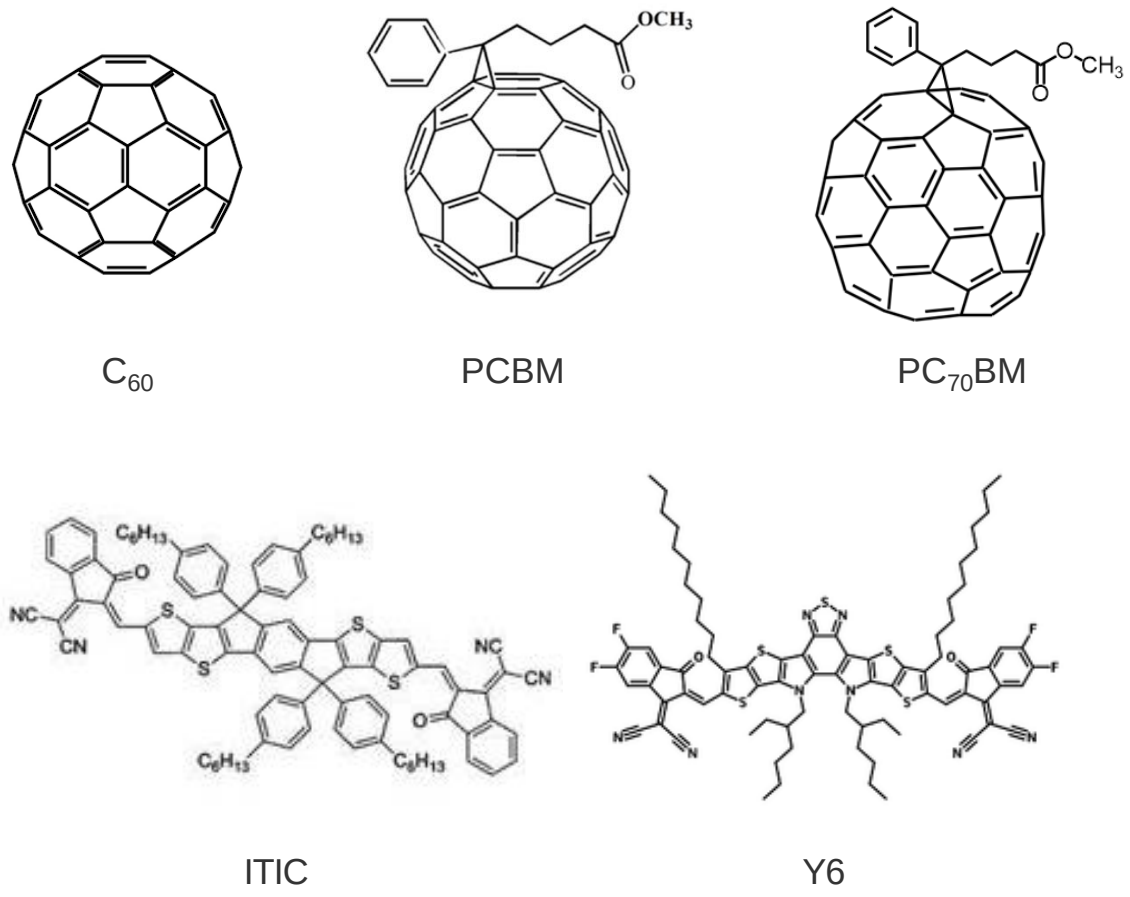

Figure 1.5.2 Chemical structure of the acceptors

1.5.3 Ambipolar molecule

An ambipolar molecule shows high hole and electron mobility in a single material. Diindenoperylene (DIP) has been reported as an ambipolar molecule [47]. Using a doping technique, *p*- and *n*- type organic semiconductors were realized using the ambipolar molecule as a host material [17].

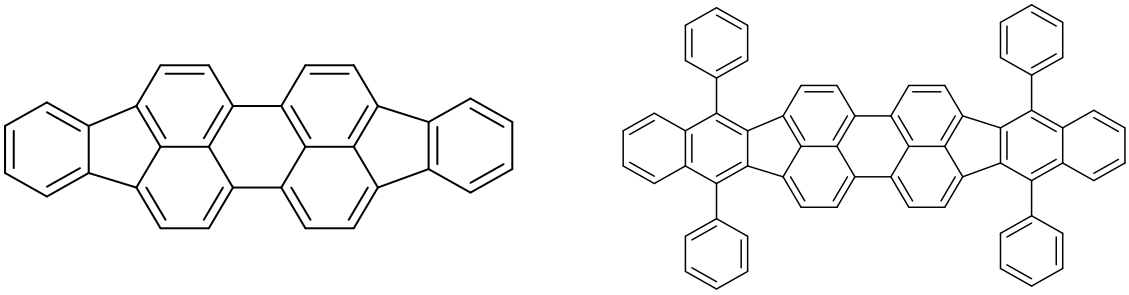

DIP DBP

Figure 1.5.3 Chemical structure of the ambipolar molecules

1.6 Current issue in organic solar cells

The power conversion efficiency of organic solar cells is introduced with three important factors, short-circuit current density, open-circuit voltage, and fill factor. In recent years, the development of non-fullerene acceptors has led to the fact that the photocurrent density of OSCs increased over 20 mA cm^{-2} and EQE reached 80%; note that the photocurrent density of OSCs is close to the performance of inorganic solar cells[48,49]. Recently, researchers focused on enhancing V_{OC} to increase the efficiency of OSCs. V_{OC} is determined by the HOMO–LUMO energy gap between the donor and acceptor, and the energy loss. CT state is the idea to examine the recombination process, and charge recombination energy loss affects voltage loss of OSCs. The development of organic solar cells requires the elucidation of the mechanism of charge recombination.

1.7 Motivation of this thesis

In this study, the author focused on the charge recombination process at the interface in OSCs.

First, typical D/A type OSCs are fabricated by different organic semiconductors that cause charge separation using the energy offset between both molecules; however, the offset is highlighted as a reason for voltage loss. Therefore, the author fabricated organic *pn*-homojunction solar cells by using single organic materials, such as inorganic solar cell structures, to induce charge separation without a typical energy offset. The Fermi level of the organic semiconductor is shifted by doping the organic semiconductor; therefore, the organic semiconductors can be changed to *p*- or *n*-type. Clarifying the correlation between the doping effect of organic *pn*-homojunction and the photoconversion mechanism suggests a new approach for improving the efficiency of solar cells.

Next, the author presents an advanced approach to examine the recombination mechanism in typical D/A type OSCs. The *J*–*V* curve of OSCs contains the information of OSCs, including charge recombination. Therefore, the author focused on observing the recombination mechanism directly from OSCs in operation. However, the method simultaneously measures the voltage dependence of photocurrent and CT state emission. The result of voltage dependence of CT state emission contains information on radiative recombination. Thus, it can consider charge separation and recombination at the D/A interface and predict the ideal *J*–*V* curve.

1.8 Overview of this thesis

This thesis comprises four chapters.

In chapter 1, the fundamental knowledge of OSCs and the motivation of this study are introduced. Thus, the photoconversion process, the device performance of OSCs, and recombination issues are described.

In chapter 2, organic *pn*-homojunction solar cells are described. The author fabricated organic *pn*-homojunction solar cells using a single material. It was able to adjust that the Fermi level of organic semiconductors using the doping effect. It was able to adjust that the Fermi level of organic semiconductors using the doping effect. Organic *pn*-homojunction was produced by Fermi-level alignment when *p* and *n*-type doped layers were contacted. Ambipolar molecule: diindinoperylene (DIP) was used as a host material for *pn*-homojunction devices. The doping concentration was controlled between 1% and 5% by volume rate, and the same concentrations of dopants (both MoO_3 and Cs_2CO_3) were introduced in the *p* and *n* layers, respectively. As a result, the J_{SC} of the DIP device with 5% doping increased eight times from the undoped one; however, V_{OC} decreased from 1.13 to 0.83 V.

The temperature dependence of *J*–*V* characteristics was measured to investigate the charge generation and recombination process. The activation energy during charge separation of 1% and 5% doped devices was calculated to be 110 and 74.4 meV, respectively. Moreover, the effective bandgap energy of 1% and 5% doped devices were calculated to be 1.95 and 1.75 eV, respectively. The result of the temperature dependence

of V_{OC} shows that the decrease in V_{OC} due to increasing doping concentration can be caused by the reduction in the effective energy gap (E_g^{eff}) at the interface.

The concentration dependence of energy diagrams suggests that the offset in adjacent molecules increases with increase in doping concentration. The larger energy offset both accelerated exciton dissociation and suppressed geminate recombination from the charge transfer (CT) state. Furthermore, the temperature dependence of V_{OC} revealed that the V_{OC} difference in the doping concentration was attributed to the E_g^{eff} difference, and not to the recombination loss difference. E_g^{eff}, which is the primary difference between inorganic and organic semiconductors, reflects the energy of the charge recombination center. However, this study shows that the charge recombination in the organic *pn*-homojunction SCs occurs from localized holes and electrons at the two adjacent molecules.

In chapter 3, the radiative recombination emission from the CT state under different applied voltages was measured at the same time as the photocurrent density flowing over the OSC device. The author introduced the concept "PL–*V* plot" in which the intensities of the recombination emission are plotted at a different applied voltage. The plot includes information from the radiative recombination, excluding the non-radiative recombination, and is complementary to the "*J*–*V* plot." The bulk heterojunction (BHJ) devices were fabricated by a well-studied combination of PTB7 as an electron donor and PCBM as an acceptor material.

Under the open-circuit to short-circuit, the radiative recombination from the CT state was estimated. The CT state emission spectra gradually decreased and disappeared

with an applied voltage of <0.5 V. The CT state emission was quenched by the internal electric field.

The FF of the two plots was calculated as 49.81% and 71.73% in *J*–*V* and PL–*V*, respectively. Thus, the result indicated that additional recombination that the PL-*V* plot cannot detect occurs when the OSC device was operated.

The FF of both plots shows different behavior when the irradiated light intensity was controlled from 100% to 10%. The FF of the *J*–*V* plots monotonically decreased from 66.7% to 49.8% when the light intensity was increased from 10% to 100%, whereas the FF of the PL–*V* plots remained constant at >70% regardless of light intensity. The result shows that the recombination that causes FF difference between the *J*–*V* and the PL–*V* plots was sensitive to the light intensity and promoted at a high carrier concentration condition and the *J*–*V* plot has a large influence at a high carrier concentration and smaller internal electric field close to the V_{OC}. Furthermore, the PL–*V* plot is a method that directly observes the CT state recombination only at the D/A interface. Therefore, the PL–*V* plot could predict the ideal FF, which considers only the characteristics of charge separation and recombination at the D/A interface and it is higher than that of *J*–*V* plots.

The temperature dependence of the CT state emission intensity has expressed the thermal quenching formula because non-radiative recombination rates are thermally activated, and the calculated activation energy from the Arrhenius plot is 64.9 meV. This result shows the vibration modes of the CT state existed between intermolecular and intra-molecular vibration.

In Chapter 4, a summary of this thesis, the conclusion, and prospects drawn from it are presented.

1.9 reference

[1] Kearns, D., Calvin, M.: Photovoltaic Effect and Photoconductivity in Laminated Organic Systems. J. Chem. Phys. 29, 950–951 (1958)

[2] C.W. Tang, Two-layer organic photovoltaic cell, Appl. Phys. Lett. 48 (1986) 183–185. doi:10.1063/1.96937.

[3] Hiramoto, M., Suezaki, M., Yokoyama, M.: Effect of thin gold interstitial-layer on the photovoltaic properties of tandem organic solar cell. Chem. Lett. (1990)19, 327–330

[4] M. Hiramoto, H. Fujiwara, M. Yokoyama, Three-layered organic solar cell with a photoactive interlayer of codeposited pigments, Appl. Phys. Lett. 58 (1991) 1062–1064. doi:10.1063/1.104423.

[5] A. You, M.A.Y. Be, I. In, Organic Solar Cells Having a Co-Deposited Interlayer of Pigments, 3781 (2003).

[6] F.. W. N . S . Sariciftci , L . Smilowitz , A . J . Heeger, Photoinduced Electron Transfer from a Conducting Polymer to Buckminsterfullerene Author (s): N . S . Sariciftci , L . Smilowitz , A . J . Heeger , F . Wudl Published by : American Association for the Advancement of Science Stable URL : http://www.jstor., Adv. Sci. 258 (2009) 1474–1476.

[7] Yu, G., Gao, J., Hummelen, J.C., Wudl, F., Heeger, A.J.: Polymer photovoltaic cells: enhanced efficiencies via a network of internal donor-acceptor heterojunctions. Science 270, 1789–1790 (1995)

[8] E. Bundgaard, F.C. Krebs, Low band gap polymers for organic photovoltaics, Sol. Energy Mater. Sol. Cells. 91 (2007) 954–985.doi:10.1016/j.solmat.2007.01.015.

[9] E. Zhou, J. Cong, K. Hashimoto, K. Tajima, A benzoselenadiazole-based low band gap polymer: Synthesis and photovoltaic application, Macromolecules. 46 (2013) 763–768. doi:10.1021/ma302596k.

[10] K. Vandewal, Z. Ma, J. Bergqvist, Z. Tang, E. Wang, P. Henriksson, K. Tvingstedt, M.R. Andersson, F. Zhang, Quantification of quantum efficiency and energy losses in low bandgap polymer: Fullerene solar cells with high open-circuit voltage, Adv. Funct. Mater. 22 (2012) 3480–3490. doi:10.1002/adfm.201200608.

[11] Y. Lin, J. Wang, Z.G. Zhang, H. Bai, Y. Li, D. Zhu, X. Zhan, An electron acceptor challenging fullerenes for efficient polymer solar cells, Adv. Mater. 27 (2015) 1170–1174. doi:10.1002/adma.201404317.

[12] A. Laventure, G.C. Welch, A tetrachlorinated molecular non-fullerene acceptor for high performance near-IR absorbing organic solar cells, J. Mater. Chem. C. 6 (2018) 9060–9064. doi:10.1039/c8tc02701c.

[13] H. Bin, Z.G. Zhang, L. Gao, S. Chen, L. Zhong, L. Xue, C. Yang, Y. Li, Non-Fullerene Polymer Solar Cells Based on Alkylthio and Fluorine Substituted 2D-

Conjugated Polymers Reach 9.5% Efficiency, J. Am. Chem. Soc. 138 (2016) 4657–4664. doi:10.1021/jacs.6b01744.

[14] K. Harada, A.G. Werner, M. Pfeiffer, C.J. Bloom, C.M. Elliott, K. Leo, Organic homojunction diodes with a high built-in potential: Interpretation of the current-voltage characteristics by a generalized einstein relation, Phys. Rev. Lett. 94 (2005) 1–4. doi:10.1103/PhysRevLett.94.036601.

[15] N. Ishiyama, M. Kubo, T. Kaji, M. Hiramoto, Doping-based control of the energetic structure of photovoltaic co-deposited films, Appl. Phys. Lett. 99 (2011) 1–4. doi:10.1063/1.3643045.

[16] C.K. Chan, W. Zhao, S. Barlow, S. Marder, A. Kahn, Decamethylcobaltocene as an efficient n-dopant in organic electronic materials and devices, Org. Electron. 9 (2008) 575–581. doi:10.1016/j.orgel.2008.03.003.

[17] S. Izawa, A. Perrot, J.H. Lee, M. Hiramoto, Organic pn homojunction solar cell, Org. Electron. Physics, Mater. Appl. 71 (2019) 45–49. doi:10.1016/j.orgel.2019.04.039.

[18] C. Ohashi, S. Izawa, Y. Shinmura, M. Kikuchi, S. Watase, M. Izaki, H. Naito, M. Hiramoto, Hall Effect in Bulk-Doped Organic Single Crystals, Adv. Mater. 29 (2017). doi:10.1002/adma.201605619.

[19] M. Hiramoto, M. Kikuchi, S. Izawa, Parts-per-Million-Level Doping Effects in Organic Semiconductor Films and Organic Single Crystals, Adv. Mater. 31 (2019) 1–15. doi:10.1002/adma.201801236.

[20] M. Kikuchi, S. Izawa, N. Rai, M. Hiramoto, Very low activation energy for carrier generation of surface doped organic single crystals observed by Hall effects, Appl. Phys. Lett. 115 (2019) 1–5. doi:10.1063/1.5116300.

[21] S.E. Shaheen, C.J. Brabec, N.S. Sariciftci, F. Padinger, T. Fromherz, J.C. Hummelen, 2.5% Efficient Organic Plastic Solar Cells, Appl. Phys. Lett. 78 (2001) 841–843. doi:10.1063/1.1345834.

[22] M. Knupfer, Exciton binding energies in organic semiconductors, Appl. Phys. A Mater. Sci. Process. 77 (2003) 623–626. doi:10.1007/s00339-003-2182-9.

[23] T.M. Clarke, J.R. Durrant, Charge Photogeneration in Organic Solar Cells, Chem. Rev. 110 (2010) 6736–6767. doi:10.1021/cr900271s.

[24] K. Vandewal, S. Himmelberger, A. Salleo, Structural factors that affect the performance of organic bulk heterojunction solar cells, Macromolecules. 46 (2013) 6379–6387. doi:10.1021/ma400924b.

[25] S. Gélinas, T.S. Van Der Poll, G.C. Bazan, R.H. Friend, Ultrafast Long-Range Charge Photovoltaic Diodes, 512 (2014) 512–517. doi:10.1126/science.1246249.

[26] B.M. Savoie, A. Rao, A.A. Bakulin, S. Gelinas, B. Movaghar, R.H. Friend, T.J. Marks, M.A. Ratner, Unequal partnership: Asymmetric roles of polymeric donor and fullerene acceptor in generating free charge, J. Am. Chem. Soc. 136 (2014) 2876–2884. doi:10.1021/ja411859m.

[27] N.A. Ran, J.A. Love, C.J. Takacs, A. Sadhanala, J.K. Beavers, S.D. Collins, Y. Huang, M. Wang, R.H. Friend, G.C. Bazan, T.Q. Nguyen, Harvesting the Full Potential of Photons with Organic Solar Cells, Adv. Mater. 28 (2016) 1482–1488. doi:10.1002/adma.201504417.

[28] J. Gorenflot, M.C. Heiber, A. Baumann, J. Lorrmann, M. Gunz, V. Dyakonov, C. Deibel, Nongeminate recombination in neat P3HT and P3HT:PCBM blend films, J. Appl. Phys. 115 (2014). doi:10.1063/1.4870805.

[29] C.M. Proctor, M. Kuik, T.Q. Nguyen, Charge carrier recombination in organic solar cells, Prog. Polym. Sci. 38 (2013) 1941–1960. doi:10.1016/j.progpolymsci.2013.08.008.

[30] T.M. Burke, S. Sweetnam, K. Vandewal, M.D. McGehee, Beyond Langevin recombination: How equilibrium between free carriers and charge transfer states determines the open-circuit voltage of organic solar Cells, Adv. Energy Mater. 5 (2015) 1–12. doi:10.1002/aenm.201500123.

[31] M. Kuik, L.J.A. Koster, G.A.H. Wetzelaer, P.W.M. Blom, Trap-assisted recombination in disordered organic semiconductors, Phys. Rev. Lett. 107 (2011) 1–5. doi:10.1103/PhysRevLett.107.256805.

[32] R.A. Street, M. Schoendorf, A. Roy, J.H. Lee, Interface state recombination in organic solar cells, Phys. Rev. B - Condens. Matter Mater. Phys. 81 (2010) 1–12. doi:10.1103/PhysRevB.81.205307.

[33] D. Credgington, F.C. Jamieson, B. Walker, T.Q. Nguyen, J.R. Durrant, Quantification of geminate and non-geminate recombination losses within a solution-processed small-molecule bulk heterojunction solar cell, Adv. Mater. 24 (2012) 2135–2141. doi:10.1002/adma.201104738.

[34] B. Qi, J. Wang, Fill factor in organic solar cells, Phys. Chem. Chem. Phys. 15 (2013) 8972–8982. doi:10.1039/c3cp51383a.

[35] B. Kippelen, J.L. Brédas, Organic photovoltaics, Energy Environ. Sci. 2 (2009) 251–261. doi:10.1039/b812502n.

[36] N. Karl, Karl03Sm, Synth. Met. 134 (2003) 1–9. papers://dc5b7a66-c191-4125-90d3-2536c98d4438/Paper/p1651.

[37] A.K. Ghosh, D.L. Morel, T. Feng, R.F. Shaw, C.A. Rowe, A. Schottky-barrier, C.A.R. Jr, Photovoltaic and rectification properties of Al/Mg phthalocyanine/Ag Schottkybarrier cells Photovoltaic and rectification properties of All Mg, J. Appl. Phys. 45 (1974) 230–236.

[38] A.K. Ghosh, T. Feng, Merocyanine organic solar cells Merocyanine organic solar cells, Appl. Phys. Lett. 49 (1978) 5982.

[39] E. Zhou, M. Nakamura, T. Nishizawa, Y. Zhang, Q. Wei, K. Tajima, C. Yang, K. Hashimoto, Synthesis and photovoltaic properties of a novel low band gap polymer based on N-substituted dithieno[3,2-b:2′3′-d]pyrrole, Macromolecules. 41 (2008) 8302–8305. doi:10.1021/ma802052w.

[40] D. Mühlbacher, M. Scharber, M. Morana, Z. Zhu, D. Waller, R. Gaudiana, C. Brabec, High photovoltaic performance of a low-bandgap polymer, Adv. Mater. 18 (2006) 2884–2889. doi:10.1002/adma.200600160.

[41] S. Foster, F. Deledalle, A. Mitani, T. Kimura, K.B. Kim, T. Okachi, T. Kirchartz, J. Oguma, K. Miyake, J.R. Durrant, S. Doi, J. Nelson, Electron collection as a limit to polymer:PCBM solar cell efficiency: Effect of blend microstructure on carrier mobility and device performance in PTB7:PCBM, Adv. Energy Mater. 4 (2014) 1–12. doi:10.1002/aenm.201400311.

[42] B. Ebenhoch, S.A.J. Thomson, K. Genevičius, G. Juška, I.D.W. Samuel, Charge carrier mobility of the organic photovoltaic materials PTB7 and PC71BM and its influence on device performance, Org. Electron. 22 (2015) 62–68. doi:10.1016/j.orgel.2015.03.013.

[43] C.T. Lee, C.H. Lee, Conversion efficiency improvement mechanisms of polymer solar cells by balance electron-hole mobility using blended P3HT:PCBM:pentacene active layer, Org. Electron. 14 (2013) 2046–2050. doi:10.1016/j.orgel.2013.04.038.

[44] J.T. Bell, G.T. Mola, Improved charge transport in P3HT:PCBM bulk heterojunction PV cell under ambient environment, Phys. B Condens. Matter. 437 (2014) 63–66. doi:10.1016/j.physb.2013.12.034.

[45] J. Yuan, Y. Zhang, L. Zhou, G. Zhang, H.L. Yip, T.K. Lau, X. Lu, C. Zhu, H. Peng, P.A. Johnson, M. Leclerc, Y. Cao, J. Ulanski, Y. Li, Y. Zou, Single-Junction Organic Solar Cell with over 15% Efficiency Using Fused-Ring Acceptor with Electron-Deficient Core, Joule. 3 (2019) 1140–1151. doi:10.1016/j.joule.2019.01.004.

[46] L. Zhan, S. Li, T.K. Lau, Y. Cui, X. Lu, M. Shi, C.Z. Li, H. Li, J. Hou, H. Chen, Over 17% efficiency ternary organic solar cells enabled by two non-fullerene acceptors working in an alloy-like model, Energy Environ. Sci. 13 (2020) 635–645. doi:10.1039/c9ee03710a.

[47] M. Horlet, M. Kraus, W. Brütting, A. Opitz, Diindenoperylene as ambipolar semiconductor: Influence of electrode materials and mobility asymmetry in organic field-effect transistors, Appl. Phys. Lett. 98 (2011) 1–4. doi:10.1063/1.3598423.

[48] S. Zhang, Y. Qin, J. Zhu, J. Hou, Over 14% Efficiency in Polymer Solar Cells Enabled by a Chlorinated Polymer Donor, Adv. Mater. 30 (2018) 1–7. doi:10.1002/adma.201800868.

[49] J. Hou, O. Inganas, R.H. Friend, F. Gao, Organic solar cells based on non-fullerene acceptors, Nat. Mater. 17 (2018) 119–128. doi:10.1038/NMAT5063.

Chapter 2: Photoconversion mechanism at the *pn*-homojunction interface in single organic semiconductor

"Photoconversion mechanism at the *pn*-homojunction interface in single organic semiconductor" Ji-Hyun Lee, Armand Perrot, Masahiro Hiramoto, Seiichiro Izawa, *Materials*. **13**, 1-8 (2020).

2.1 Abstract

Clarifying critical differences in free charge generation and recombination processes between inorganic and organic semiconductors is important for developing efficient organic photoconversion devices such as solar cells (SCs) and photodetector. In this study, the author analyzed the dependence of doping concentration on the photoconversion process at the organic *pn*-homojunction interface in a single organic semiconductor by using temperature dependence of *J*-*V* characteristics and energy structure measurements. Even though the organic *pn*-homojunction SC devices were fabricated by using a single host material and the doping technique resembling an inorganic *pn*-homojunction, the charge generation and recombination mechanisms are similar to that of conventional Donor/Acceptor (D/A) type organic SCs: the charge separation happens from localized exciton and charge transfer (CT) state being separated by the energy offset between adjacent molecules, and the recombination happens from localized charge carrier at two adjacent molecules. The determining factor for photoconversion processes is the localized nature of charges in organic semiconductors. The results demonstrated that controlling the delocalization of the charges is important to realize efficient organic photoconversion devices.

2.2 Introduction

Free charge generation processes by light absorption in inorganic and organic semiconductors are completely different. Inorganic semiconductors have a large dielectric constant; thus, free charges are directly formed after the light absorption in a single semiconductor material [1]. In contrast, a strongly bounded Frenkel type exciton forms after light absorption in organic semiconductors because they generally have a smaller dielectric constant when compared to that of inorganic semiconductors [2]. The exciton can be separated by using the energy offset between the two organic semiconductor materials called donor and acceptor in organic solar cells (OSCs) [2,3]. The question is whether free charge formation is possible in single organic semiconductor material by light absorption, similar to that in inorganic semiconductors.

Recently, S.Izawa, et.al. have reported that *pn*-homojunction interfaces in a single organic semiconductor films formed by doping can achieve efficient charge separation [4]. The organic *pn*-homojunction solar cell SC device showed a high internal quantum efficiency of 30%. Further investigation for clarifying the mechanism of the photoconversion at the *pn*-homojunction interface can help to answer the basic question how free charges form beyond the strong coulomb binding and recombine in a single organic semiconductor film, and what is the critical difference in these processes between organic and inorganic semiconductors.

In this study, the author analyzed the doping concentration dependence on the photoconversion process in organic *pn*-homojunction SC devices mainly by a temperature dependence measurement. The measurement gives information about thermal activation for the charge generation and recombination pathways [5,6]. Upon combining an energy

structure measurement near the *pn*-homojunction, the author revealed the detailed mechanism of photoconversion at the single organic semiconductor interface.

2.3 Experimental

Device fabrication

The OSC devices were fabricated on ITO-coated glass substrates (ITO thickness: 150 nm; sheet resistance: 10.3 Ω sq^{-1}; Techno Print). MoO_3 (Alfa Aesar), DIP (Lumtec), Cs_2CO_3 (Sigma-Aldrich), BCP (Tokyo Chemical Industry) were used without further purification.

The MoO_3 hole-transporting layer (10 nm, 0.1 nm s^{-1}), doped DIP layer (100 nm, 0.1 nm s^{-1}), BCP electron-transport layer (15 nm, 0.1 nm s^{-1}), and Al electrodes (60 nm, 0.4 nm s^{-1}) were deposited via thermal evaporation under high vacuum (~10^{-5} Pa) in a vacuum evaporation system (VTS-350M, ULVAC) housed in a glove box (UNICO). The MoO_3 and Cs_2CO_3 as the dopants were introduced by co-deposition with DIP.

Device characteristics

The devices were characterized in a vacuum container for optical measurements (Epitech) without exposure to air. The *J*–*V* characteristics of the devices were measured under simulated solar illumination (AM 1.5, 100 mW cm^{-2}) from a solar simulator based on a 300-W Xe lamp (HAL-320, Asahi Spectra) using a source meter (R6243, Advantest). The light intensity was calibrated with a standard silicon solar cell (CS-20, Asahi Spectra) and controlled by neutral density filter (SIGMAKOKI). The active area of the devices was defined using a 0.04 cm^2 photomask. The EQE values of the devices were measured using a monochromator (SPG-100 ST, Shimadzu), a 500W Xe lamp (UI-502Q, Ushio Lighting), and a silicon photodiode (Hamamatsu Photonics). The *J*–*V* characteristics of

the devices at various temperatures were measured in a cryostat (Janis) without exposure to air.

The UV-vis absorption spectra were measured on a spectrometer (V-570, JASCO). The PYS spectra were measured using an (AC-2, RIKEN KEIKI). The W_F was determined using a Kelvin probe (FAC-1, Riken-Keiki) without exposure to air. The Kelvin probe was housed in a glove box with N_2 gas (H_2O < 1 ppm, O_2 < 1 ppm).

The X-ray diffraction patterns were measured on a powder X-ray diffractometer (RINT-UltimaIII, Rigaku). The X-ray wavelength of Cukα is 1.5406Å.

2.4 Result and discussion

2.4.1 Device fabrication and characteristics

The *pn*-homojunction SC devices were fabricated in the same manner as previously reported [4]. the author used diindenoperylene (DIP) which is an ambipolar organic semi-conductor molecule as the host, and MoO_3 and Cs_2CO_3 as *p*- and *n*-dopants, respectively. The device was fabricated by thermal evaporation under high vacuum, and the structure was indium tin oxide (ITO)/MoO_3: 10 nm/ MoO_3-doped DIP: 50 nm/ Cs_2CO_3-doped DIP: 50 nm/bathocuproine (BCP): 10 nm/Al: 60 nm (**Figure. 2.4.1**). Dopants were introduced into the semiconductor layer via co-deposition techniques and the concentration of the dopants relative to the semiconductor volume were controlled by varying the ratio between the deposition rates of the two species [4]. **Figure 2.4.2** shows the typical *J-V* characteristics of *pn*-homojunction devices. As previously reported, J_{SC} drastically increased and V_{OC} decreased with an increase in doping concentration. The degrees of J_{SC} increase were 8 times from undoped to 5% doping in the DIP devices. In previous study, S. Izawa, et.al have reported that the device with 10% doping showed

lower J_{SC} [4]. That reason might be attributed to the deteriorative effect of high doping concentration. It explained that the DIP active layer with high doping concentration showed the quenching of excitons after photoexciation. In contrast, V_{OC} decreased from 1.13 V to 0.83 V. The FF values increased marginally in the device with high doping concentration. The increase of external quantum efficiency (EQE) spectra without the change in spectral shape (**Figure 2.4.3**) indicated that charge separation from the absorption of the ground state of DIP was accelerated by doping.

The previous study also confirmed the effect of *pn*-homojunction interface on photoconversion by combination of the doped and undoped layer in the device [4]. J_{SC} with *p*-doped/undoped and undoped/*n*-doped layer was measured. The result showed similar J_{SC} result as for whole undoped device. Only the device with *pn*-homojunction interface demonstrated a significant increase in J_{SC}. The result indicated *pn*-homojunction interface should be necessary for efficient photogeneration when using single organic semiconductor. **Figure 2.4.4** shows the X-ray diffraction (XRD) of undoped (black), MoO_3 5% doped (green) and Cs_2CO_3 5% doped (purple) DIP thin films. The thin films were fabricated at 50 nm on silicon substrate. It has already been reported that the DIP molecules form edge-on orientation and lattice constant is estimated about 16.5 Å [20]. The result of XRD spectra also show high crystallinity. (001) peak shows the highest intensity and other (00n) peaks are ovserved clearly. The c-axis length of undoped DIP thin film is 16.6 Å, which is the same as other doped thin films. This result indicates that each DIP molecule is arranged at equal intervals in the vertical direction regardless of doping, and sugessts that the energy shift at the *pn*-interface can be described by the energy gap between adjacent molecules.

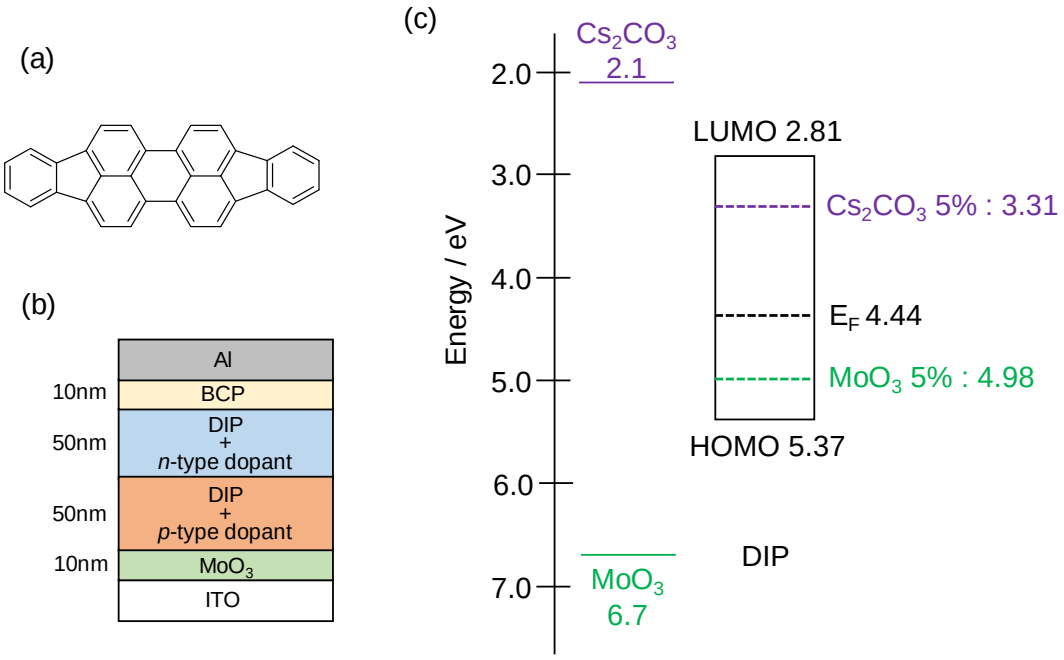

Figure 2.4.1 (a) Chemical structure of DIP. (b) Schematic of the *pn*-homojunction device. (c) Energy levels of DIP, MoO_3 and Cs_2CO_3. The dashed lines indicate the position of E_F of the 50 nm undoped (black), 5% MoO_3 doped (green) and 5% Cs_2CO_3 doped (purple) films on ITO substrates.

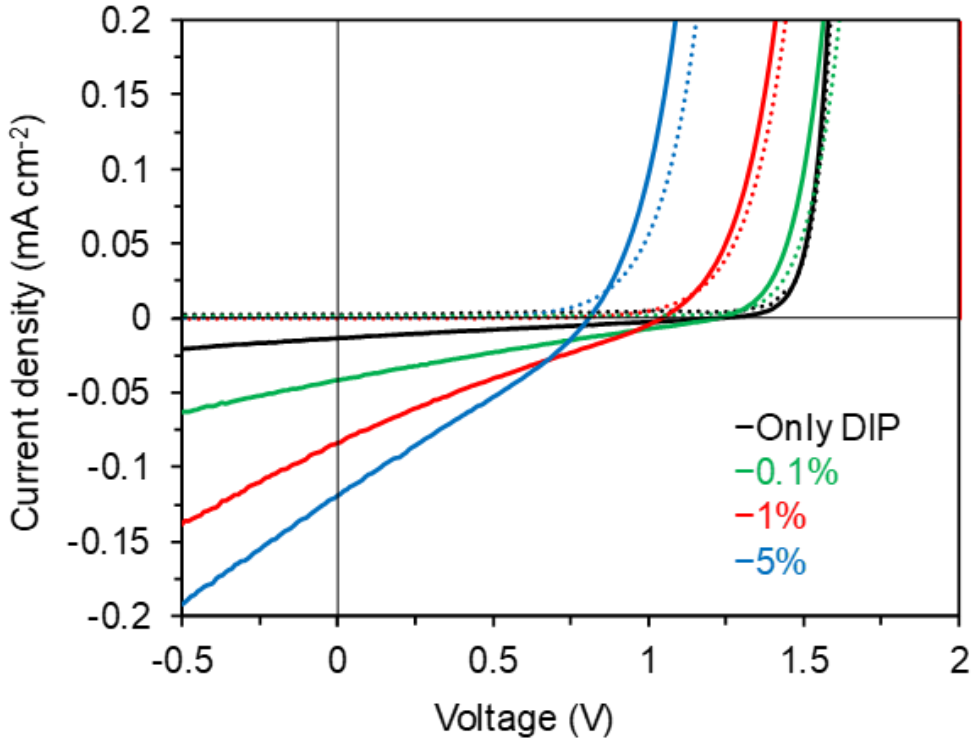

Figure 2.4.2. *J*–*V* curves of homojunction devices with 100 nm undoped layer (black) and *pn* doped DIP layers having same MoO_3 and Cs_2CO_3 concentrations of 0.1% (green), 1% (red) and 5% (blue) using DIP as a host molecule under AM 1.5 irradiation (100mW cm^{-2}, solid lines) or in the dark (dashed lines). The same concentrations of *p*- and *n*-dopants were introduced in the active layers.

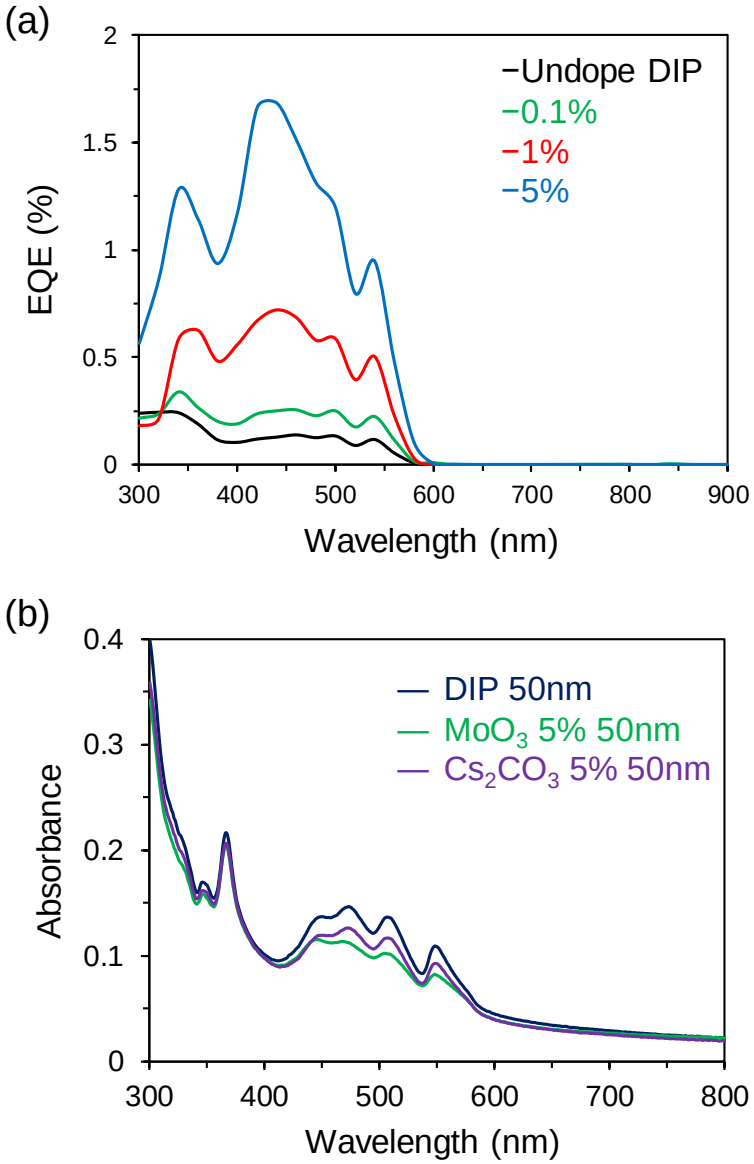

Figure 2.4.3. (a) EQE spectra of homojunction devices with undoped DIP layer (black), and *pn* doped DIP layers with same MoO_3 and Cs_2CO_3 concentrations of 0.1% (green), 1% (red) and 5% (blue). (b) Absorption spectra of undoped (dark blue), 5% MoO3 doped (green) and 5% Cs2CO3 doped (purple) DIP films on quartz. The amount of DIP on quartz is equivalent to 50 nm in all the films.

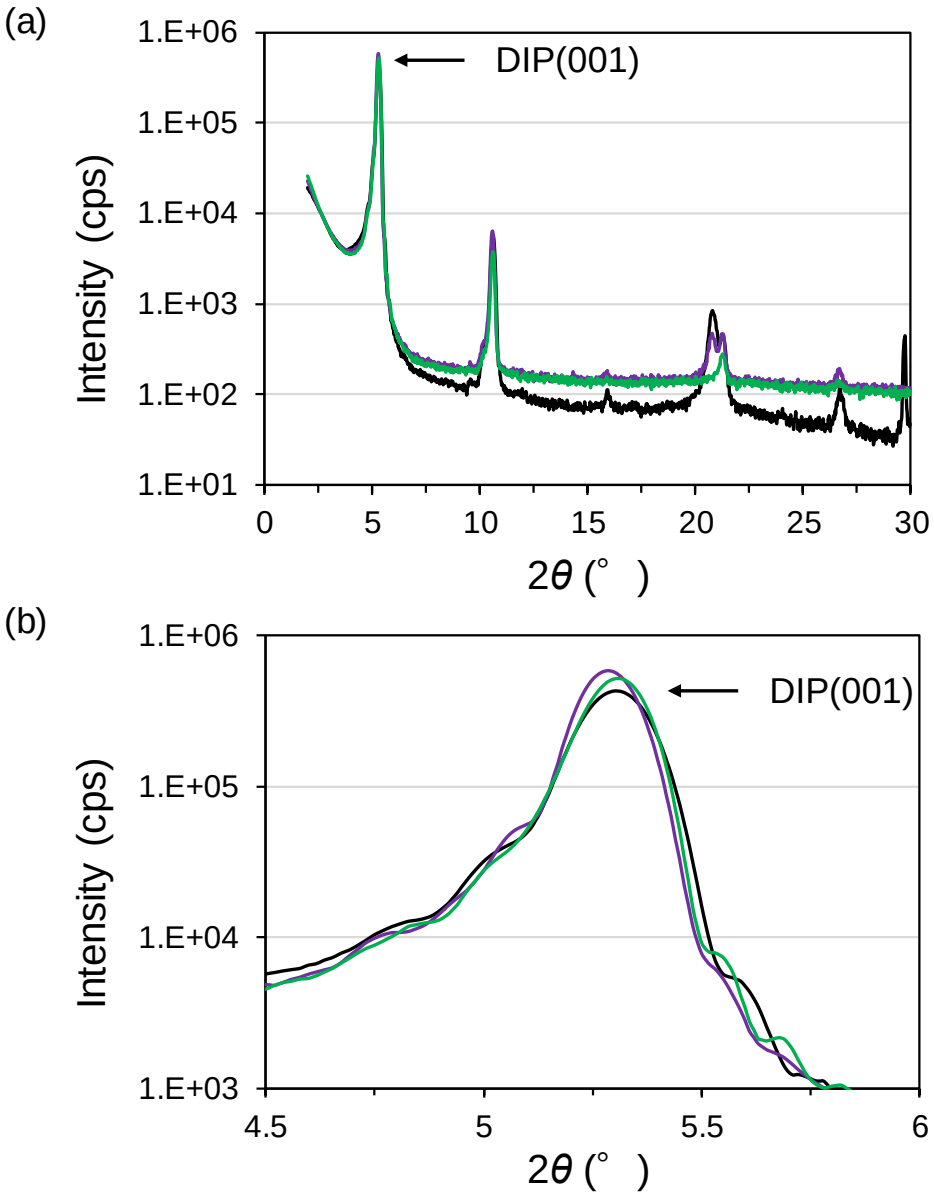

Figure 2.4.4 (a) XRD spectra of out of plane of undoped (black), MoO_3 doped (green) and Cs_2CO_3 doped (purple) DIP thin film. (b) Zoom of first specular of DIP Bragg reflection.

2.4.2 Temperature dependence of J_{SC} and V_{OC} of *pn*-homojunction OSC

To investigate the charge generation and recombination processes, the author measured the *J-V* characteristics of the devices at temperatures from 30 to −60 °C as shown in **Figure 2.4.5.** Typically, J_{SC} decreases while V_{OC} increases with a decrease in temperature in the OSCs [6]. The *pn*-homojunction devices followed the same tendency. Firstly, the temperature dependence of J_{SC} is expressed by the following Arrhenius equation:

$$J_{SC} = J_0(P_{light}) \exp(-E_a/kT) \qquad \text{equation 2.4.1}$$

where $J_0(P_{light})$ is the pre-exponential factor, E_a is the activation energy, k is Boltzmann constant and T is temperature [7]. The origin of E_a was attributed to the activation process during charge separation [5,8]. The calculated E_a of the devices with 5% and 1% doped DIP from the Arrhenius plots in **Figure 2.4.6 (a)** are 74.4 and 110 meV, respectively. The 5% doped device showed a lesser E_a than 1% doped, indicating that the charge separation was accelerated in the device with high doping concentration.

Next, the temperature dependence of V_{OC} is expressed by the following equation:

$$qV_{OC} = E_g^{eff} - nkTln(\frac{J_{00}}{J_{ph}}) \qquad \text{equation 2.4.2}$$

where q is elementary charge, E_g^{eff} is effective bandgap energy at the interface, n is ideality factor, J_{ph} is the photogenerated current density, and J_{00} is the pre-exponential factor of the reverse saturation current density [ref. 9]. E_g^{eff} is the bandgap of inorganic semiconductor in the case of inorganic solar cell and the CT state energy in the case of organic solar cell. Equation 2.4.2 represents the V_{OC}, which is determined by temperature

dependent two parts: the former energetic term and the latter recombination loss term [6]. The V_{OC} plots as a function of temperature are shown **Figure 2.4.6 (b)**. E_g^{eff} of the devices with 5% and 1% doped DIP calculated from the intercept of the plots are 1.75 and 1.95 eV, respectively. On the other hand, the V_{OC} loss values induced by the recombination: $E_g^{eff}/q - V_{OC}$ of the both devices showed similar values of 0.95 and 0.92 V, respectively. The results indicate that the decrease in V_{OC} due to an increase in doping concentration is due to the reduction in the effective energy gap at the interface, not due to the difference in the recombination processes.

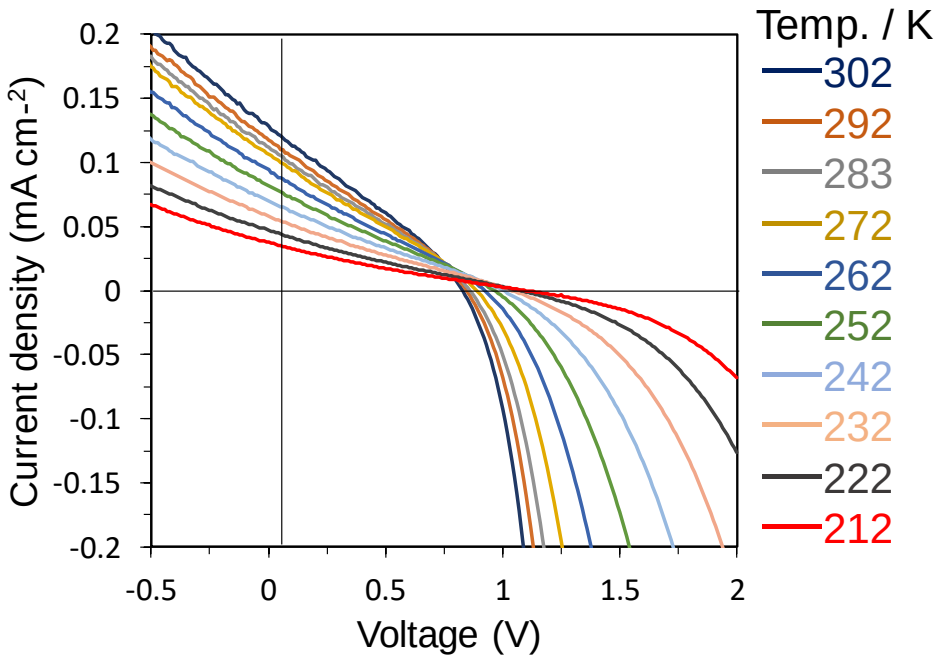

Figure 2.4.5. *J*-*V* curves for the 5% doped *pn*-homojunction device at various temperatures under AM 1.5 irradiation (100 mW cm^{-2}).

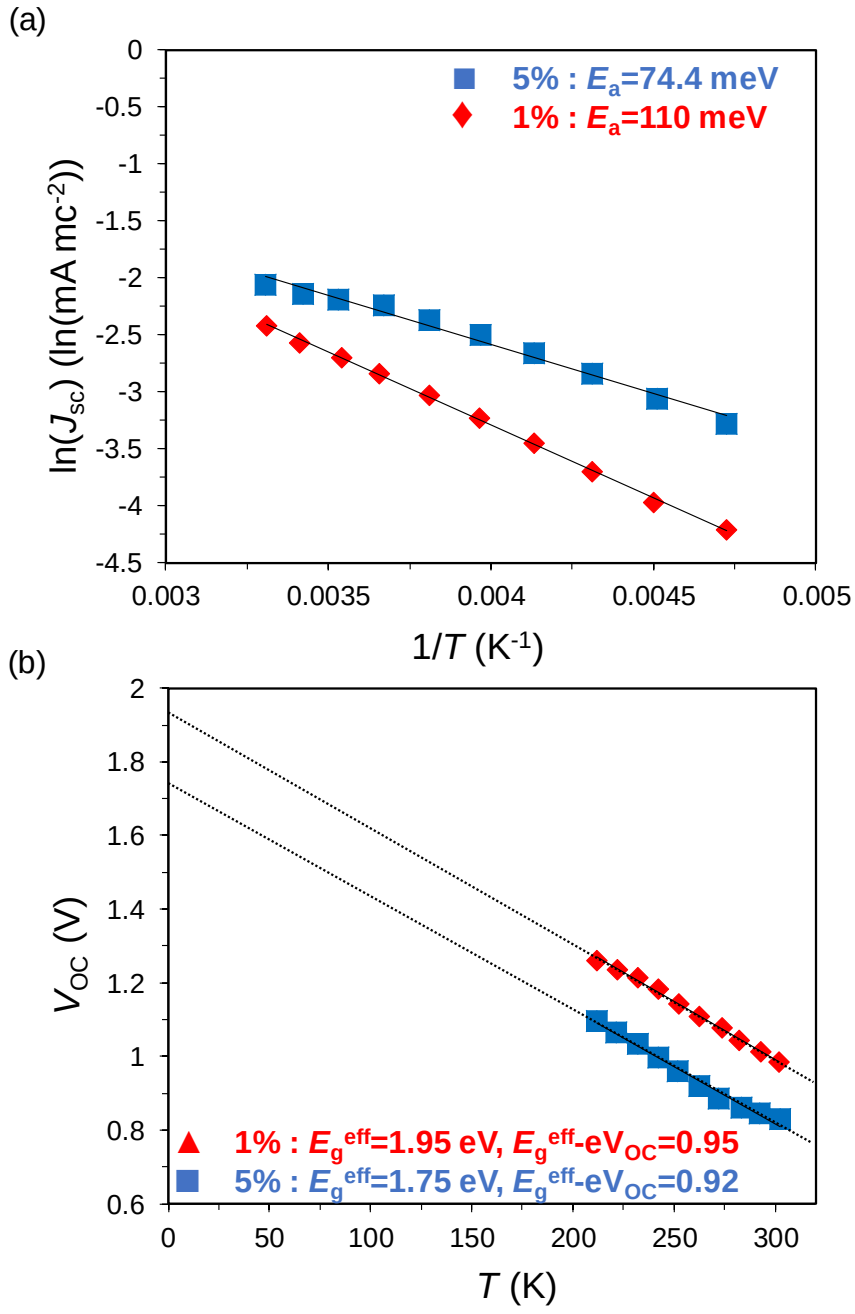

Figure 2.4.6. Temperature dependence of (a) J_{SC} and (b) V_{OC} for the 1% doped (red) and 5% doped (blue) *pn*-homojunction devices.

2.4.3 The energetic structure in *pn*-interface

The energetic structure of the doped DIP films was estimated by energy-level mapping using the Kelvin probe (KP) method to measure the work function (WF) [10–12]. **Figure 2.4.7** shows schematic image of the KP measurement. A metal prove is brought close to the surface of the sample to be measured, and the contact potential gap due to the difference in work function between the sample and the probe is measured. The work function of the sample surface can be obtained by using a probe with a known work function. In this study, Author used the ITO substrate as a standard sample and the work function of ITO substrate is 4.7 eV. **Figure 2.4.8** is the result of energy shift at the *pn*-interface of the 5% doped DIP film. And the results of the 1% doped DIP film are shown in **Figure 2.4.9**. The WF of the *p*-doped layer was measured on an Al/BCP/*n*-doped layer substrate and that of *n*-doped layer was measured on an ITO/MoO_3/*p*-doped layer substrate, because to calculate doping concentration dependence of the energy shift at the *pn*-interface. The steep change in the WF near the *pn*-interface was observed in all the films. The ionization potentials (IP) of the undoped and doped DIP films were evaluated by photoelectron yield spectroscopy (PYS) in **Figure 2.4.10**. The IPs of the undoped and doped films did not change significantly, indicating that doping does not affect the IP of the films. Small changes in the absorption spectra (ABS) shown in **Figure 2.4.3 (b)** also indicate that the bandgap and electron affinity (EA) of the film were not affected by doping. Therefore, the energetic structure of doped DIP films was determined only by the WF difference [10].

The energy diagrams of the active layer in the *pn*-homojunction devices were estimated based on the result of the KP measurement [13]. The drawback of the KP

measurement is that it can only measure the WF at the surface of the films. the author cannot observe the WF change of the underlying layer after the deposition of the over layer. To estimate the energetic structure of whole films, the author calculated the electric potential distribution derived from Poisson's equation [13]. The total depletion layer width (*W*) of *pn*-junction for uniformly doped semiconductor is given by the following equation:

$$W = \sqrt{\frac{2\varepsilon\varepsilon_0 V_{bi}(N_p^- + N_n^+)}{qN_p^- N_n^+}} \qquad \text{equation 2.4.3}$$

$$qN_{\mathrm{n}}^- x_{\mathrm{p}} = qN_{\mathrm{n}}^+ x_{\mathrm{n}} \qquad \text{equation 2.4.4}$$

$$W = x_{\mathrm{p}} + x_{\mathrm{n}} \qquad \text{equation 2.4.5}$$

where ε, ε_0, V_{bi}, N_{n}^-, N_{p}^+, x_{p}, and x_{n} denote the relative dielectric constant of the semi-conductor, the dielectric permittivity in a vacuum, the built-in-potential, ionized dopant concentration of *p* and *n* layer, and the depletion layer width in the *p*- and *n*-type regions, respectively. The N_{p}^+ and N_{n}^- values can be calculated by the measured x_{p}, x_{n} and V_{bi} values in **Figure 2.4.8 and 2.4.9**. The ionized charge concentration N_{p}^+ and N_{n}^- of 5% doped device are 2.80×10^{18} and 2.49×10^{18} cm^{-3}, respectively, and the doping efficiency of both *p* and *n* dopants are 0.75% and 0.67%. In the same way, N_{p}^+ and N_{n}^- of 1% doped device are 2.20×10^{17} and 1.51×10^{17} cm^{-3}, respectively, and the doping efficiency of *p* and *n* dopants are 1.18% and 0.81%. For 5% doped devices, the amount of charge that can be doped have already saturated. The electric potential distribution V(x) at the *pn*-junction can be found by integrating Poisson's equation as follows.

$$V(x) = -\frac{qN_n^+}{2\varepsilon_r\varepsilon_0}(x + x_n)^2 + V_{bi}\ (-x_n \leqq x \leqq 0) \qquad \text{equation 2.4.6}$$

$$V(x) = \frac{qN_p^-}{2\varepsilon_r\varepsilon_0}\left(x_p - x\right)^2 \ (0 \leqq x \leqq x_p) \qquad \text{equation 2.4.7}$$

Figure 2.4.11 shows the calculated energy diagram of the active layer in the *pn*-homo-junction devices. The *W* and V_{bi} values of the 5% and 1% doped DIP devices are 20 nm, 1.40 eV and 60 nm, 0.99 eV, respectively. This shows that the higher doping concentration decreased the W value and increased the V_{bi} value.

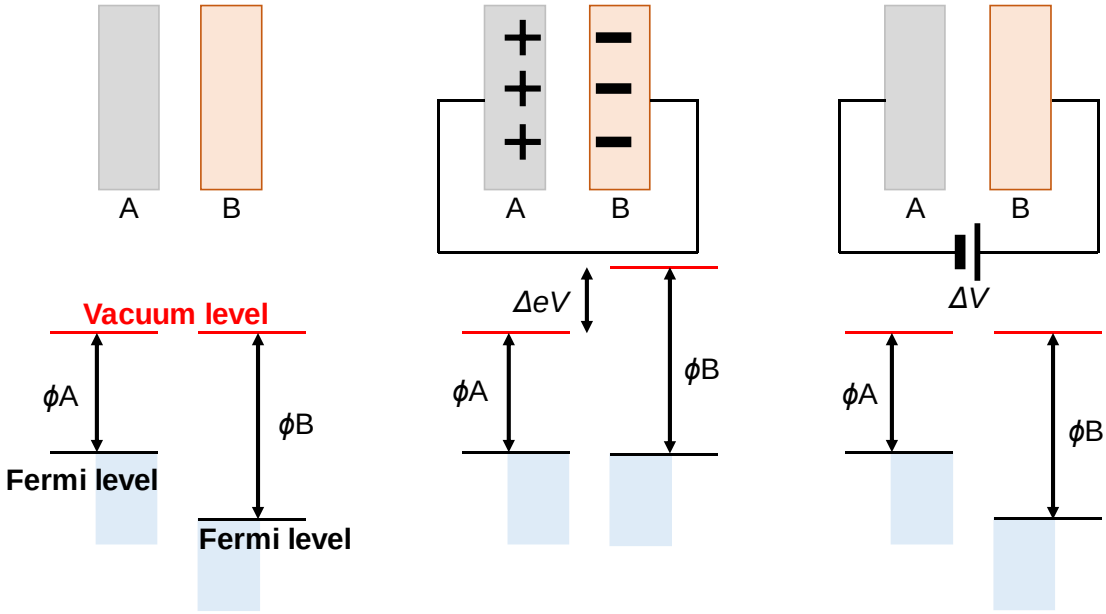

Figure 2.4.7. Schematic of Kelvin probe method

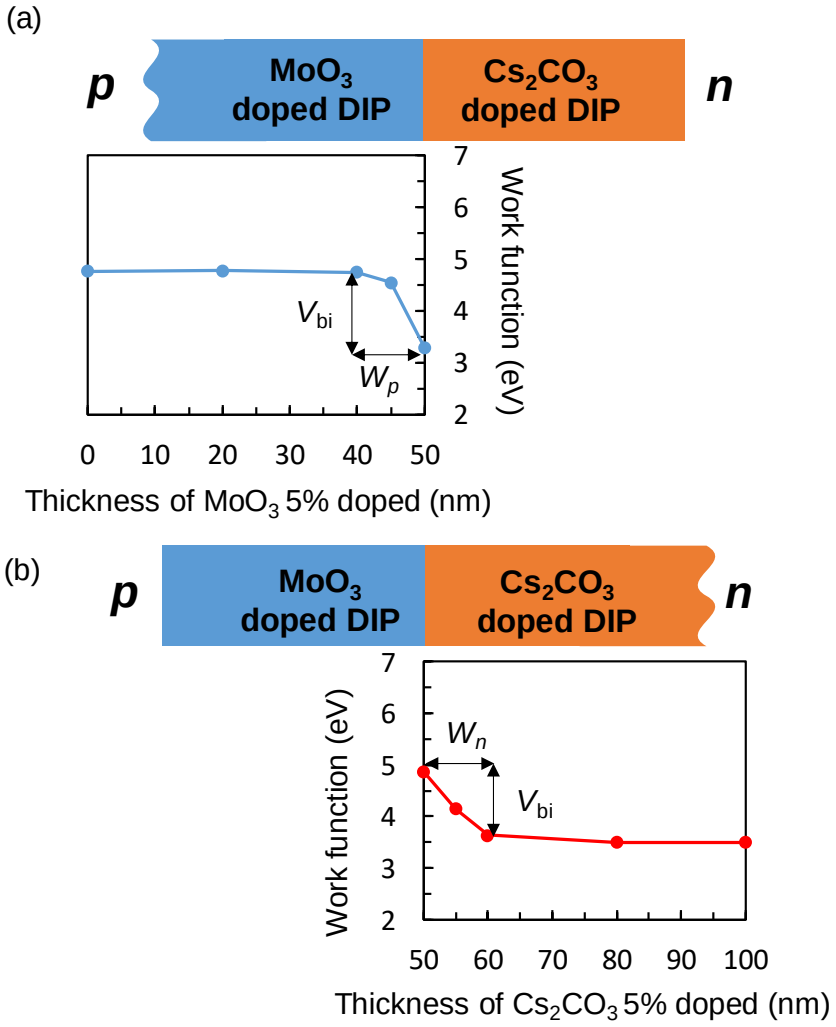

Figure 2.4.8. WF of (a) 5% MoO_3 doped and (b) 5% Cs_2CO_3 doped DIP films on the Cs_2CO_3 doped film and the MoO_3 doped film, respectively, as a function of the thickness.

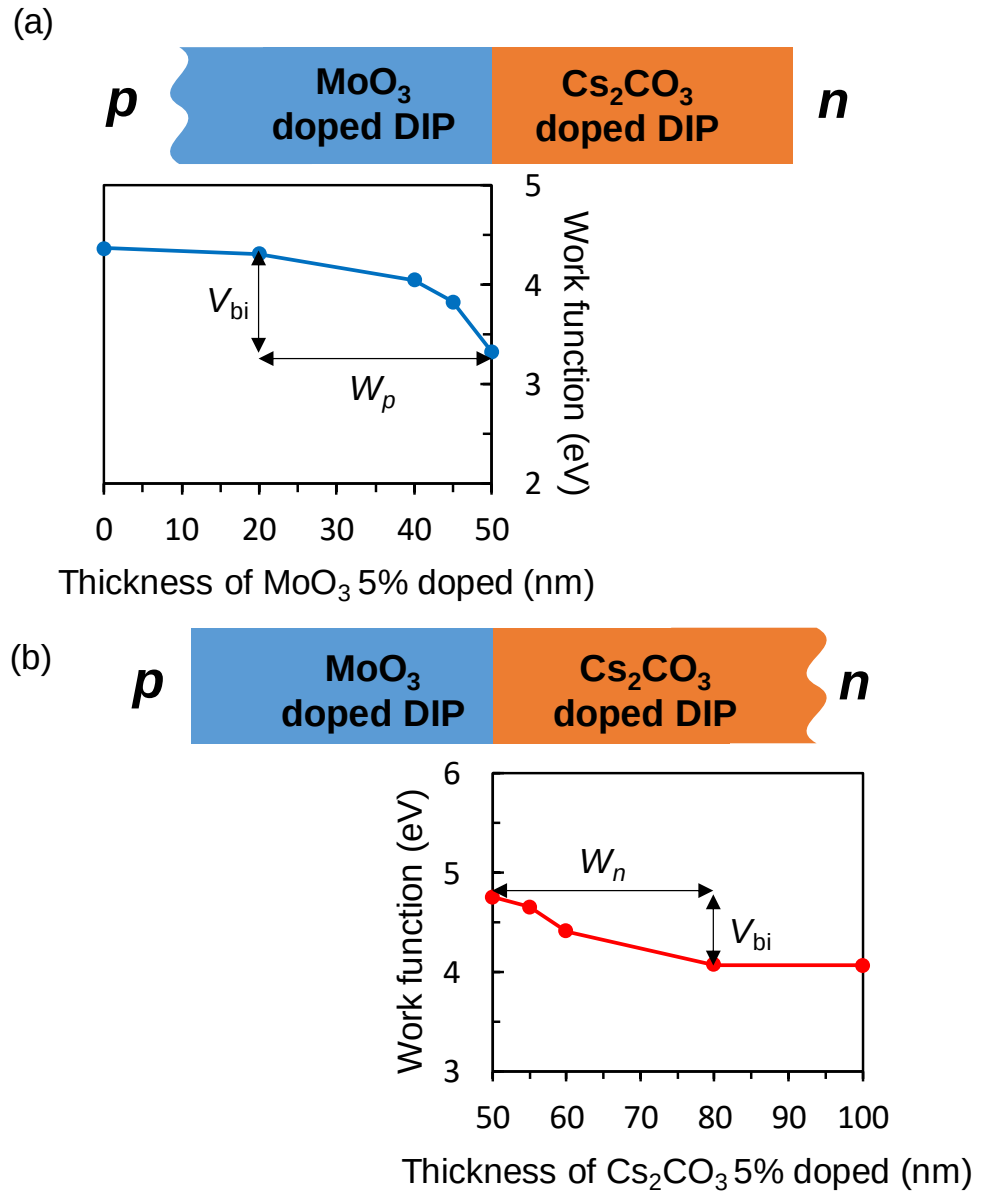

Figure 2.4.9. W_F of (a) 1% MoO_3 doped and (b) 1% Cs_2CO_3 doped DIP films on the Cs_2CO_3 doped film and the MoO_3 doped film, respectively, as a function of the thickness.

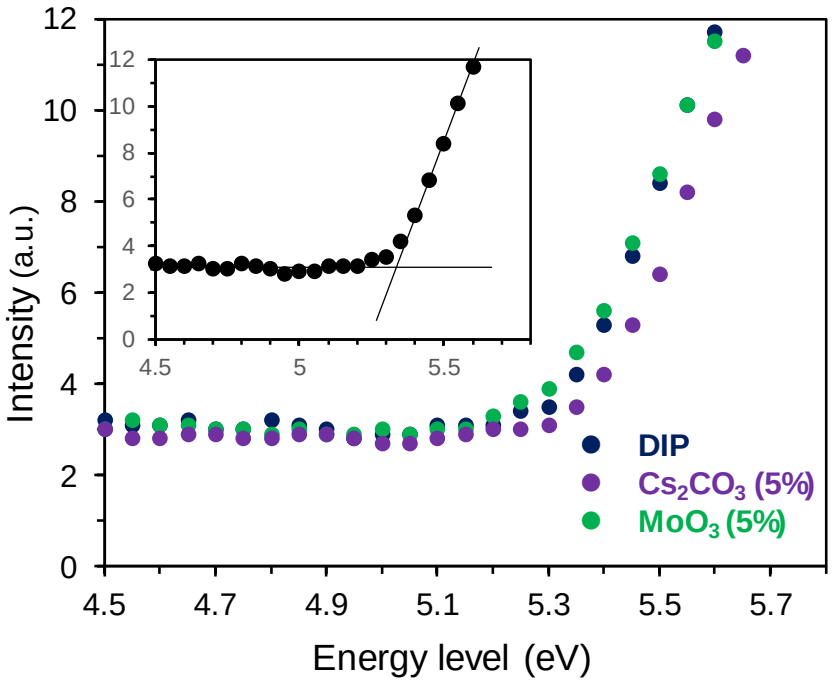

Figure 2.4.10. Photoelectron yield spectra of undoped DIP (dark blue), Cs_2CO_3 5% doped DIP (purple) and MoO_3 5% doped DIP (green) thin film. Ionic potential is estimated by approximate line of plot.

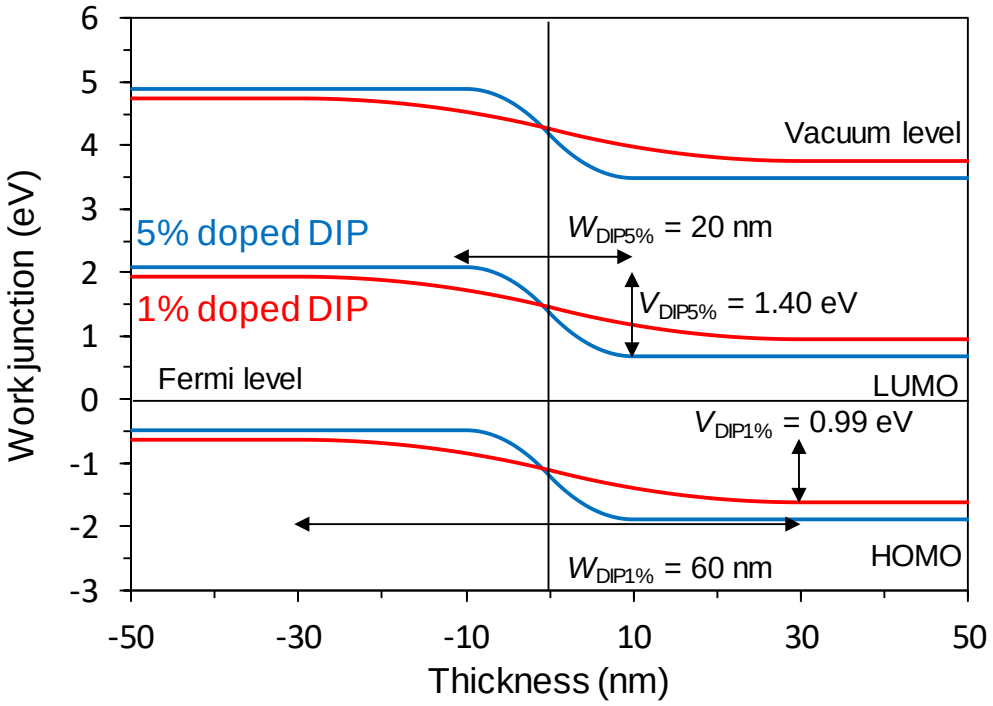

Figure 2.4.11. Vacuum level, HOMO, and LUMO energy levels relative to the Fermi level in the 1% doped DIP (red) and 5% doped DIP (blue) devices as a function of film thickness. These results are based on the KP measurement shown in **Figure 2.4.8 and 2.4.9** and the calculation by equation 2.4.6 and 2.4.7.

2.4.4 Charge dissociation and recombination mechanisms in organic *pn*-interface

The charge generation and recombination processes in the *pn*-homojunction devices are discussed based on the results of the temperature dependence of *J*-*V* characteristics and the energy structure measurements. Firstly, J_{SC} increased 8 times due to doping and E_a for charge separation decreased from 110 meV in the 1% doped *pn*-homojunction devices to 74.4 meV in the 5% doped *pn*-homojunction devices. In this study, the author used the same host material, and only the interfacial energetics were modified by the doping. The light intensity dependence of J_{SC} in the 1% and 5% doped devices in **Figure 2.4.12** showed that the slopes of both the devices were close to unity, indicating that the bimolecular recombination is negligible under a short circuit condition [14]. Thus, the origin of the difference in the E_a induced by doping is attributed to the charge separation process and not to the exciton diffusion nor the bimolecular recombination process. The charge separation processes are mainly separated into the two processes: exciton to CT state, which is defined as a bounded charge pair by the coulomb attraction at the interface, and the CT state to the charge separated state [2]. The energy structure measurement revealed that the energy offset between adjacent molecules at the *pn*-interface was 0.07 and 0.26 eV for 1% and 5% doped devices, respectively. The offset at one molecular layer apart from the *pn*-interface was 0.06 and 0.22 eV in the 1% and 5% doped devices, respectively (**Figure 2.4.13**). The conventional donor/acceptor (D/A) type OSCs have an energy offset only at the D/A interface, and an offset larger than 0.3 eV not only accelerates the exciton dissociation but also suppresses geminate recombination from the CT state [15]. By the analogy with the D/A type OSCs, the energy

offset between adjacent molecules at the *pn*-interface is crucial for charge separation in the *pn*-homojunction devices. The reason for smaller E_a in the 5% doped device, compared to that in the 1% device, was that larger energy offset close to 0.3 eV in the 5% doped device not only accelerated exciton dissociation but also suppressed geminate recombination from the CT state.

In contrast to J_{SC}, V_{OC} decreased from 0.98 V in the 1% to 0.83 V in the 5% doped devices. Temperature dependence of V_{OC} revealed that the V_{OC} difference in the doping concentration was attributed to the E_g^{eff} difference, not to the recombination loss difference. E_g^{eff} reflects the energy of charge recombination center [16]. In the case of inorganic SCs, E_g^{eff} corresponds to the energy of the bandgap of the semiconductor material because the charge recombination happens from delocalized charges on the conduction and valence bands [16]. In contrast, E_g^{eff} in the conventional D/A type OSCs corresponds to the CT state energy because localized electrons on the LUMO of acceptor and holes on the HOMO of donor recombine [17]. In the case of the organic *pn*-homojunction SCs in this study, E_g^{eff} decreased with an increase of V_{bi}. E_g^{eff} difference between 1% and 5% is 0.20 eV that is almost same value with the energy offset difference between 1% and 5% at the adjacent molecules at the *pn*-interface (**Figure 2.4.13**). The result indicates that the charge recombination in the organic *pn*-homojunction SCs happens from localized holes and electrons at the two adjacent molecules. The mechanism is similar to that of the CT state recombination in the conventional D/A type OSCs, even though the devices in this study were fabricated by using a single host material and a doping technique resembling the inorganic *pn*-homojunction SCs.

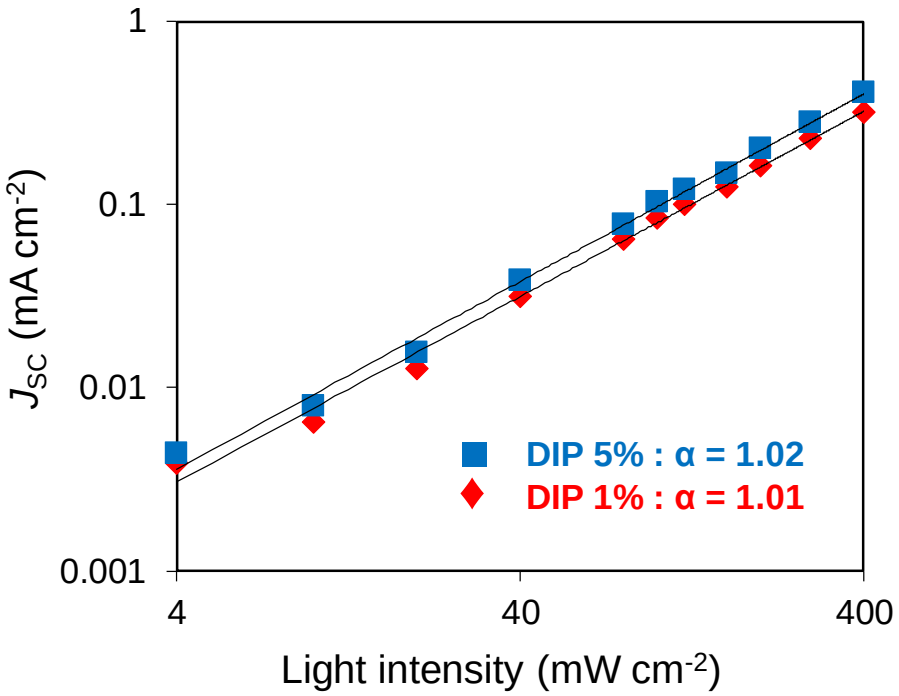

Figure 2.4.12 Light intensity dependence of J_{SC} of the devices with the 1% (red) and 5% (blue) doped DIP. The value of α shows the slope of approximate line.

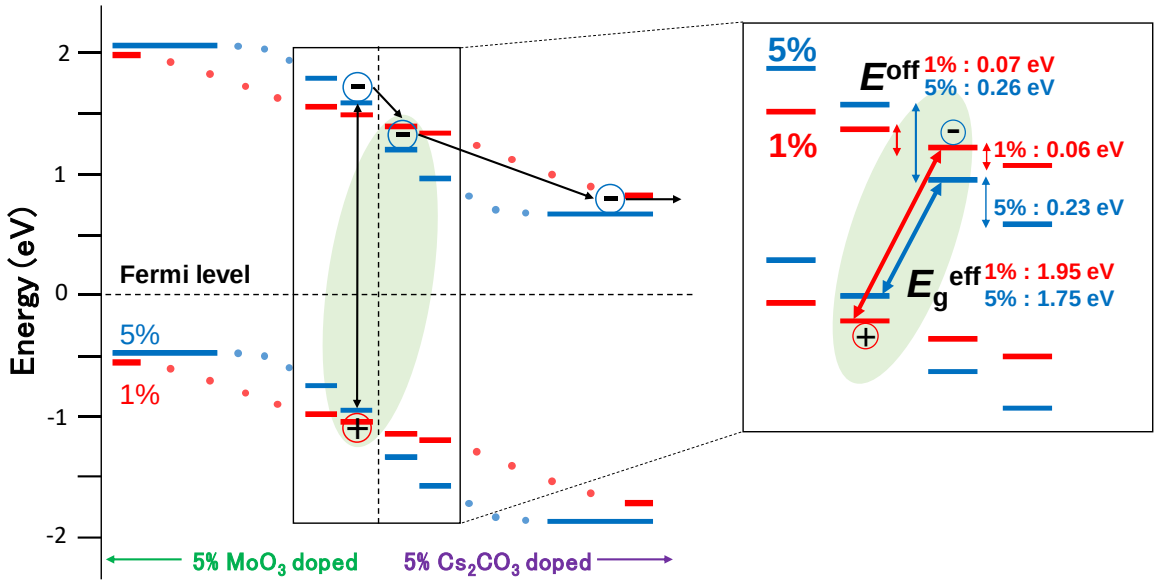

Figure 2.4.13 Schematic energy diagram and charge dissociation and recombination mechanisms in organic *pn*-homojunction SCs. The inset shows energy gap between adjacent molecules at *pn*-interface with 1% (red) and 5% (blue) doping.

2.5 Conclusion

Temperature dependence of *J*-*V* characteristics and energy structure measurement revealed that the increase in J_{SC} and decrease in V_{OC} with an increase in doping concentration in the organic *pn*-homojunction SC devices was due to the acceleration of charge separation and the change in energy of the recombination center. The charge separation mechanism in the device is that localized exciton and CT state are separated by the energy offset between adjacent molecules, and the recombination happens from the localized charge carrier at two adjacent molecules. These mechanisms are similar to those of conventional D/A type OSCs not to those of the inorganic SCs. In the case of inorganic *pn*-homojunction, larger V_{bi} formed by higher doping concentration lead to both higher J_{SC} and V_{OC} [1]. Same tendency is favorable to obtain high efficiency in organic *pn*-homojunction SCs. The primordial difference in photoconversion process between inorganic and organic *pn*-homojunction SCs comes from the delocalized and localized nature of charges in inorganic and organic semiconductors, respectively. Recently, some organic semiconductor materials showed band-like nature of charges [18,19]. Utilizing these kinds of materials as hosts in organic *pn*-homojunction SCs could realize direct free charge formation and band-to-band recombination.

2.6 References

[1] C. Battaglia, A. Cuevas, S. De Wolf, High-efficiency crystalline silicon solar cells: Status and perspectives, Energy Environ. Sci. 9 (2016) 1552–1576. doi:10.1039/c5ee03380b.

[2] T.M. Clarke, J.R. Durrant, Charge Photogeneration in Organic Solar Cells, Chem. Rev. 110 (2010) 6736–6767. doi:10.1021/cr900271s.

[3] M. Hiramoto, M. Kubo, Y. Shinmura, N. Ishiyama, T. Kaji, K. Sakai, T. Ohno, M. Izaki, Bandgap Science for Organic Solar Cells, Electronics. 3 (2014) 351–380. doi:10.3390/electronics3020351.

[4] S. Izawa, A. Perrot, J.H. Lee, M. Hiramoto, Organic pn homojunction solar cell, Org. Electron. Physics, Mater. Appl. 71 (2019) 45–49. doi:10.1016/j.orgel.2019.04.039.

[5] S. Izawa, K. Nakano, K. Suzuki, K. Hashimoto, K. Tajima, Dominant effects of first monolayer energetics at donor/acceptor interfaces on organic photovoltaics, Adv. Mater. 27 (2015) 3025–3031. doi:10.1002/adma.201500840.

[6] N. Shintaku, M. Hiramoto, S. Izawa, Effect of trap-assisted recombination on open-circuit voltage loss in phthalocyanine/fullerene solar cells, Org. Electron. Physics, Mater. Appl. 55 (2018) 69–74. doi:10.1016/j.orgel.2018.01.016.

[7] I. Riedel, V. Dyakonov, Influence of electronic transport properties of polymer-fullerene blends on the performance of bulk heterojunction photovoltaic devices, Phys. Status Solidi Appl. Res. 201 (2004) 1332–1341. doi:10.1002/pssa.200404333.

[8] F. Gao, W. Tress, J. Wang, O. Inganäs, Temperature dependence of charge carrier generation in organic photovoltaics, Phys. Rev. Lett. 114 (2015) 1–5. doi:10.1103/PhysRevLett.114.128701.

[9] S. Yamamoto, A. Orimo, H. Ohkita, H. Benten, S. Ito, Molecular understanding of the open-circuit voltage of polymer:Fullerene solar cells, Adv. Energy Mater. 2 (2012) 229–237. doi:10.1002/aenm.201100549.

[10] S. Izawa, N. Shintaku, M. Hiramoto, Effect of Band Bending and Energy Level Alignment at the Donor/Acceptor Interface on Open-Circuit Voltage in Organic Solar Cells, J. Phys. Chem. Lett. 9 (2018) 2914–2918. doi:10.1021/acs.jpclett.8b01134.

[11] H. Ishii, N. Hayashi, E. Ito, Y. Washizu, K. Sugi, Y. Kimura, M. Niwano, Y. Ouchi, K. Seki, Kelvin probe study of band bending at organic semiconductor/metal interfaces: Examination of fermi level alignment, Phys. Status Solidi Appl. Res. 201 (2004) 1075–1094. doi:10.1002/pssa.200404346.

[12] N. Shintaku, M. Hiramoto, S. Izawa, Doping for Controlling Open-Circuit

Voltage in Organic Solar Cells, J. Phys. Chem. C. 122 (2018) 5248–5253. doi:10.1021/acs.jpcc.7b12203.

[13] Y. Yamashina, Y. Shinmura, N. Ishiyama, T. Kaji, M. Hiramoto, Mapping of band-bending in organic pn -homojunctions, J. Appl. Phys. 117 (2015). doi:10.1063/1.4915506.

[14] L.J.A. Koster, M. Kemerink, M.M. Wienk, K. Maturová, R.A.J. Janssen, Quantifying bimolecular recombination losses in organic bulk heterojunction solar cells, Adv. Mater. 23 (2011) 1670–1674. doi:10.1002/adma.201004311.

[15] K. Nakano, Y. Chen, B. Xiao, W. Han, J. Huang, H. Yoshida, E. Zhou, K. Tajima, Anatomy of the energetic driving force for charge generation in organic solar cells, Nat. Commun. 10 (2019) 1–10. doi:10.1038/s41467-019-10434-3.

[16] S.S. Hegedus, W.N. Shafarman, Thin-film solar cells: device measurements and analysis, Prog. Photovoltaics Res. Appl. 12 (2004) 155–176. doi:10.1002/pip.518.

[17] T.M. Burke, S. Sweetnam, K. Vandewal, M.D. McGehee, Beyond Langevin recombination: How equilibrium between free carriers and charge transfer states determines the open-circuit voltage of organic solar Cells, Adv. Energy Mater. 5 (2015) 1–12. doi:10.1002/aenm.201500123.

[18] F. Bussolotti, J. Yang, T. Yamaguchi, K. Yonezawa, K. Sato, M. Matsunami, K. Tanaka, Y. Nakayama, H. Ishii, N. Ueno, S. Kera, Hole-phonon coupling effect on the band dispersion of organic molecular semiconductors, Nat. Commun. 8 (2017). doi:10.1038/s41467-017-00241-z.

[19] C. Liu, T. Minari, X. Lu, A. Kumatani, K. Takimiya, K. Tsukagoshi, Solution-processable organic single crystals with bandlike transport in field-effect transistors, Adv. Mater. 23 (2011) 523–526. doi:10.1002/adma.201002682.

[20] A.C. Dürr, F. Schreiber, M. Münch, N. Karl, B. Krause, V. Kruppa, H. Dosch, High structural order in thin films of the organic semiconductor diindenoperylene, Appl. Phys. Lett. 81 (2002) 2276–2278. doi:10.1063/1.1508436.

Chapter 3: Simultaneous measurement of photocurrent and recombination emission in organic solar cell

"Simultaneous measurement of photocurrent and recombination emission in organic solar cell" Ji-Hyun Lee, Masahiro Hiramoto, Seiichiro Izawa, submitted (2021).

3.1 Abstract

The charge transfer (CT) state is a key intermediate to understand the recombination processes that induce a reduction of power conversion efficiency in organic solar cells (OSCs). In this study, the author measured the recombination emission from the CT state under different applied voltages in the OSC device and a photocurrent density flowing on the circuit simultaneously. Experimentally, the author extracted only the information of CT state emission at the interface and proposed a "PL–*V* plot" that is the voltage dependence of PL intensity of the CT state. The PL–*V* plot includes information from the radiative recombination at the donor/acceptor interface and is complementary to the "*J*–*V* plot" that is the most important information for evaluating OSCs. The results demonstrated that the fill factor of the PL–*V* plot is higher than that of the *J*-*V* plot because the PL–*V* plot reports the CT state recombination at the D/A interface, predicting the ideal FF of the device. Furthermore, the value of the activation energy for the non-radiative recombination is estimated by the temperature dependence of the CT state emission intensity. Our result demonstrated that the simultaneous measurement of photocurrent and recombination emission proposed in this study could be a strong tool for evaluating photoconversion characteristics at the D/A interface in OSCs.

3.2 Introduction

Organic solar cells (OSCs) have attracted attention as a renewable energy source because of their low cost and flexibility. However, to put OSCs to practical use, the power conversion efficiency (PCE) of OSCs that have exceeded over 18% should get close to crystalline silicon SCs [1,2]. In a typical donor/acceptor (D/A) type OSCs, an exciton that is generated by light absorption is dissociated into an electron-hole pair by using an energy difference between the highest occupied molecular orbital (HOMO) and lowest unoccupied molecular orbital (LUMO) of the D/A materials, and charge transfer (CT) state that is defined as a bounded charge pair by Coulomb attraction at the D/A interface forms. Thus, free charges eventually form from the CT states after overcoming the Coulomb attraction [3]. However, a recombination process that is a deactivation, from a generated free charge to a ground state occurs through the CT state. The recombination processes are classified as radiative and non-radiative recombination. Especially, the non-radiative recombination that is induced by thermal vibration is the main problem that causes large energy loss in open-circuit voltage (V_{OC}) in OSCs [4,5]. Therefore, clarifying the mechanism that induces recombination loss is important for further improving the PCE of OSCs. In general, the CT state that is a key intermediate for recombination processes is investigated by electroluminescence (EL) measurement [6]. However, the number of charges are injected into the device by applying a relatively large forward voltage to measure EL of CT state emission due to the CT state has low emission quantum yield as low as from 10^{-3} to 10^{-5}% and small overlaps of molecular orbital between D/A materials [6]. The character of the CT state should be investigated under similar

conditions with standard SC operations, such as light irradiation and moderate applied voltages.

In this study, the author observed the radiative recombination emission from the CT state by simultaneously measuring the photocurrent density flowing on the OSC device under different applied voltages. Relationships between the amount of radiative recombination and extracted photocurrent density to the electrode under different applied voltages is as follows: in the open-circuit condition of the OSC devices, the photogenerated current density (J_{ph}), and recombination current density (J_{rec}) balances, all the generated charges are recombined via CT state [7]. Thus, photoluminescence (PL) intensity of recombination emission from the CT state was maximized, and no net current flows on the circuit. When the applied voltage goes below the V_{OC}, some free charges begin to accumulate on the electrodes, but others recombined due to insufficient electric field in the device. Therefore, the recombination emission decreases, and the photocurrent flowing in the circuit increases compared to the OC condition. In a short circuit condition, most of all CT states are separated and free charges are accumulated on the electrodes due to the large electric field. Thus, almost all of the recombination emission from the CT state is quenched. By subtracting PL spectra at short-circuiting from open-circuit, the author can extract only the information of CT state emission at the D/A interface by canceling out a background signal that is independent of the bias voltage. In addition, the author can introduce the concept `PL-*V* plot` where the intensities of the recombination emission are plotted at a different applied voltage from this observation. The plot includes the information only from the radiative recombination, excluding the non-radiative recombination, and is complementary to the `*J*-*V* plot` that is the most important information for evaluating OSCs but includes all the recombination events.

3.3 Experimental

Device fabrication

The ITO substrate was pre-cleaned in UV ozone cleaner for 20 min. A thin layer of polyethylenimine ethoxylated (PEIE) was prepared by spin-coating at 5000 rpm for 60 s on the ITO substrate. Then, PEIE film was annealed at 200 °C for 10 min in the atmosphere. The PTB7:PCBM (5:7.5 g/L) was dissolved in chloroform (CF) with the solvent additive of 1.8-diiodooctane (DIO) (3%, v/v). The solution was spin-coated at 1000 rpm for 120 s onto the PEIE layer and the thickness of the active layer was about 120 nm. The MoO_3 hole transporting layer (10 nm, 0.1 nm/s), and Ag electrode (100 nm, 0.3 nm/s) were deposited via thermal evaporation under high vacuum (~10^{-5} Pa) in a vacuum evaporation system (VTS-350M, ULVAC) housed in a glove box (UNICO). The devices were encapsulated in the glove box by a glass substrate and epoxy resin and characterized without exposure to air. The devices were placed in a cryostat for temperature dependence measurement.

Evaluation for the device performance

The *J-V* characteristics of the devices were measured under simulated solar light illumination (AM 1.5, 100 mW/cm^2) from a solar simulator based on a 300 W Xe lamp (Hal-320, Asahi Spectra) using a source meter (R6243, Adventist). The light intensity was calibrated with a standard silicon solar cell (CS-20, Asahi Spectra). The active area of the devices was defined using a 0.126 cm^2 photomask. The light intensity was controlled by a neutral density filter (AND-50S, SIGMAKOKI) in the measurement of the light intensity dependence. The highly sensitive EQE of the devices was measured on a Hypermonolight SM 250F system with an NF LI5640 lock-in amplifier (Bunkoh Keiki).

Optical measurements

The UV-vis absorption spectra were measured on a spectrometer (V-570, JASCO). The near-IR PL spectra were measured by SPEX Fluorolog 3–21 (HORIBA) with an InGaAs detector. The excitation light source was a 470 nm monochromatic LED light (LED470L, THORLABS). The bandwidth of monochromatic LED light was 22 nm. The active area of the devices was defined using a 0.126 cm^2 photomask. The *J-V* characteristics of the devices during PL experiments were measured using a source meter (Model 2450, KEITHLEY).

3.4 Result and discussion

3.4.1. Device Characteristics

The device of bulk heterojunction (BHJ) OSCs was fabricated in the configuration of the inverted structure with a well-studied combination of PTB7 as electron donor and PCBM as acceptor materials (**Figure 3.4.1 (a)**): ITO/polyethylenimine ethoxylated (PEIE)/PTB7:PCBM/MoO_3/Ag. The BHJ layer was spin-coated from the mixed solution of PTB7:PCBM by using chloroform as a solvent and 3% of 1.8-diiodooctane (DIO) as an additive [8-10]. The *J-V* characteristics of the PTB7/PCBM device under simulated solar light were presented in **Figure 3.4.1 (b)**. The value of V_{OC}, short circuit current density (J_{SC}), fill factor (FF) and PCE were obtained as 0.74 V, 13.54 mA/cm^2, 67.10%, and 6.76%, respectively. Those performances are comparable to the previous report [11]. CT state absorption and emission spectra were measured by highly sensitive EQE and EL measurements as presented in **Figure 3.4.1 (c)**. The CT state absorption and the emission peaks could be fitted by a Gaussian function based on Marcus's theory [6]. The peak centers of the CT state absorption and the emission were determined as 1.46 eV and 1.18 eV, respectively. Thus, CT state energy (E_{CT}) was determined as 1.32 eV by the intersection of the two Gaussian curves (**Figure 3.4.1 (c)**) [6].

At V_{OC}, the recombination current balances with photocurrent J_{ph} and V_{OC} is given by

$$V_{OC} = \frac{nkT}{e} \ln\left(\frac{J_{ph}}{J_0} - 1\right)$$

$$\approx \frac{nkT}{e} \ln\left(\frac{J_{ph}}{J_0}\right) \qquad \text{(equation 1.4.6)}$$

where J_0 is the dark saturation current density, J_{ph} is the photocurrent density, n is the ideality factor, k is Boltzmann's constant, T is temperature and e is the elementary charge.

Reciprocity relation between photovoltaic quantum efficiency and electroluminescent emission have been reported by Rau [6]. J_0 is related to the electro-optical properties by

$$J_0 = \frac{q}{EQE_{EL}} \int EQE_{PV}(E)\phi_{BB}^{T} dE \qquad \text{equation 3.4.1}$$

where EQE_{EL} is the electroluminescence external quantum efficiency and ϕ^{T}_{BB} is the black body spectrum at temperature T. EQE_{PV} was obtained in the spectral region of CT absorption (**Figure 3.4.1 (c)**), and the equation is given by

$$EQE_{PV}(E) = \frac{f}{E\sqrt{4\pi\lambda kT}} \exp\left(\frac{-(E_{CT}+\lambda-E)^2}{4\pi\lambda k}\right) \qquad \text{equation 3.4.2}$$

Using equation 3.4.2 in equation 3.4.1 gives

$$J_0 \approx \frac{q}{EQE_{EL}} f \frac{2\pi}{h^3c^2}(E_{CT}-\lambda)\exp\left(-\frac{E_{CT}}{kT}\right) \qquad \text{equation 3.4.3}$$

EQE_{PV} is evaluated at short-circuit, therefore the equation 1.4.6 should be evaluated with a short circuit using $J_{ph}=J_{SC}$. Using equation 3.4.3 in equation 1.4.6, The equation for V_{OC} as a function of EQE_{EL} and, energy losses due to radiative recombination ($q\Delta V_{rad}$) and non-radiative recombination ($q\Delta V_{non}$) is given by:

$$V_{OC} = \frac{E_{CT}}{q} + \frac{kT}{q}\ln\left(\frac{J_{SC}h^3c^2}{fq2\pi(E_{CT}-\lambda)}\right) + \frac{kT}{q}\ln(EQE_{EL}) \qquad \text{equation 3.4.4}$$

In analogy to Ref. 7, the energetic losses due to radiative recombination ($q\Delta V_{rad}$) and non-radiative recombination ($q\Delta V_{non}$) also estimated by the following equations:

$$q\Delta V_{rad} = -kT\ln\left(\frac{J_{SC}h^3c^2}{fq2\pi(E_{CT}-\lambda)}\right) \qquad \text{equation 3.4.5}$$

$$q\Delta V_{non} = -kT\ln(EQE_{EL}) \qquad \text{equation 3.4.6}$$

$$qV_{OC} = E_{CT} + q\Delta V_{rad} + q\Delta V_{non} \qquad \text{equation 3.4.7}$$

where λ is reorganization energy that was determined by the CT absorption measurement (Figure 3.4.1 (c)), f is the reduced absorption of CT state, h is Planck constant and c is the speed of light. The calculated energy loss of ΔV_{rad} and ΔV_{non} at room

temperature are 0.23 V and 0.34 V, respectively. And EQE_{EL} value is 1.3×10^{-6}. EQE_{EL} can be approximated to $\Delta J_{rad}/\Delta J_{non}$. This result indicated that non-radiative recombination occurs one million times more than radiative recombination.

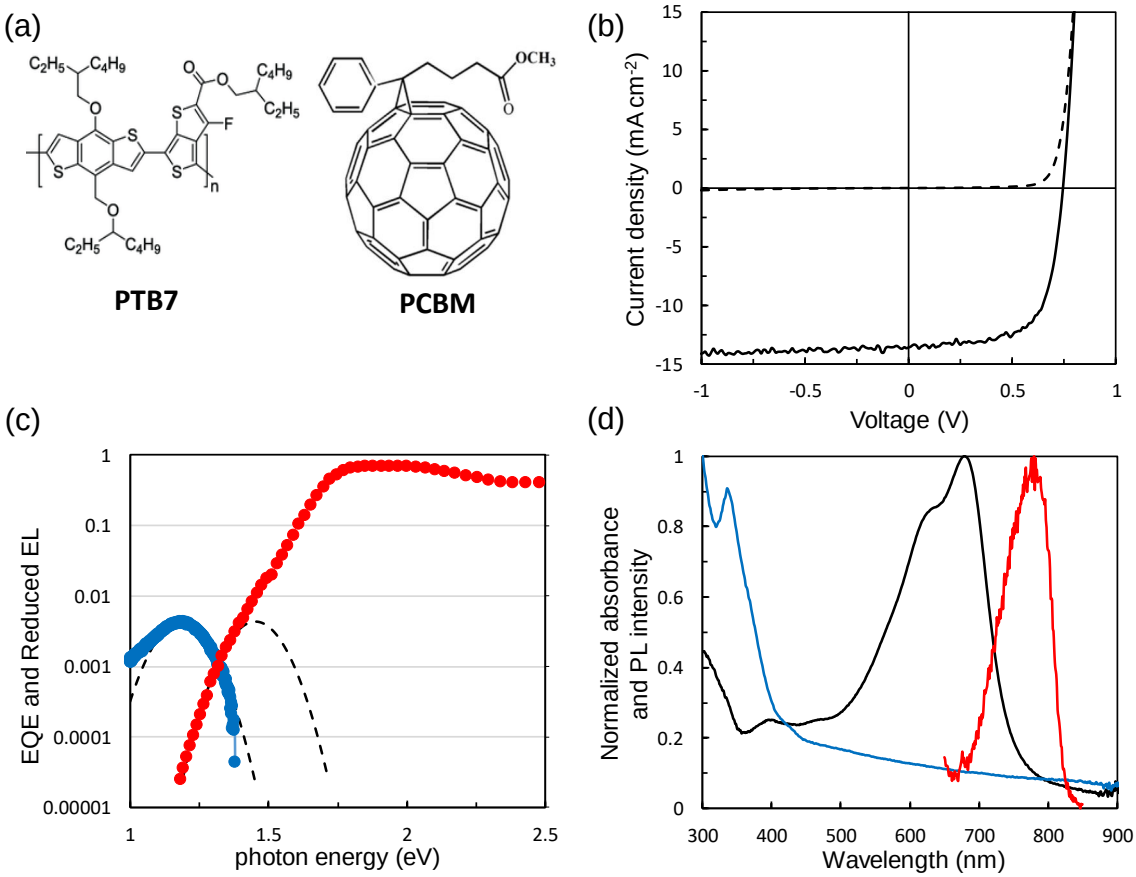

Figure 3.4.1. (a) Chemical structure of the donor (PTB7) and acceptor (PCBM) materials. (b) *J-V* curves of the PTB7/PCBM device under A. M. 1.5, 100 mW cm^{-2} irradiation and dark. (c) EQE (red) and reduced EL (blue) spectra of the PTB7/PCBM. (d) Absorption spectra of PTB7 (black), PCBM (blue) pristine film and PL spectra of PTB7 (red).

3.4.2 In-situ measurement of radiative recombination

To investigate the radiative recombination from the CT state under different applied voltages, PL spectra of PTB7/PCBM device at near-infrared region irradiated by 470 nm monochromatic LED light was measured under the open-circuit (0.75 V) to short-circuit (0 V) conditions in 0.01 V steps (**Figure 3.4.2 (a)**). The reason for choosing excitation wavelength at 470 nm was that PTB7 had small absorbance at the wavelength to reduce a fluorescence signal, and the wavelength was enough far to the NIR region where the CT state emission appears. The light intensity was set as 468 mW/cm^2 at which the device shows four times larger J_{SC} than 1 sun condition of a solar simulator. The V_{OC} of the device in this excitation condition was 0.75 V. In the PL spectrum when the V_{OC} (0.75 V) was applied, small peaks at 1.18 eV were observed in the emission tail of the fluorescence from PTB7. The peaks gradually decreased and disappeared with a smaller applied voltage than 0.5 V. The PL emission was quenched by the internal electric field, and the EL spectrum of the device in **Figure 3.4.1 (c)** revealed that the peak center of the CT state was 1.18 eV. Therefore, the author concluded the PL emission at 1.18 eV was from radiative recombination from the CT state. To separate the emission tail of the fluorescence from PTB7 and the CT state emission, the PL spectra were subtracted by the spectrum at 0 V where almost all of the CT state was quenched and only the PTB7 fluorescence that is bias independent remains. The subtracted PL spectra as **Figure 3.4.2 (b)** exhibited the peak center of CT state emission was 1.18 eV, and the emission was quenched under a smaller voltage than 0.5 V.

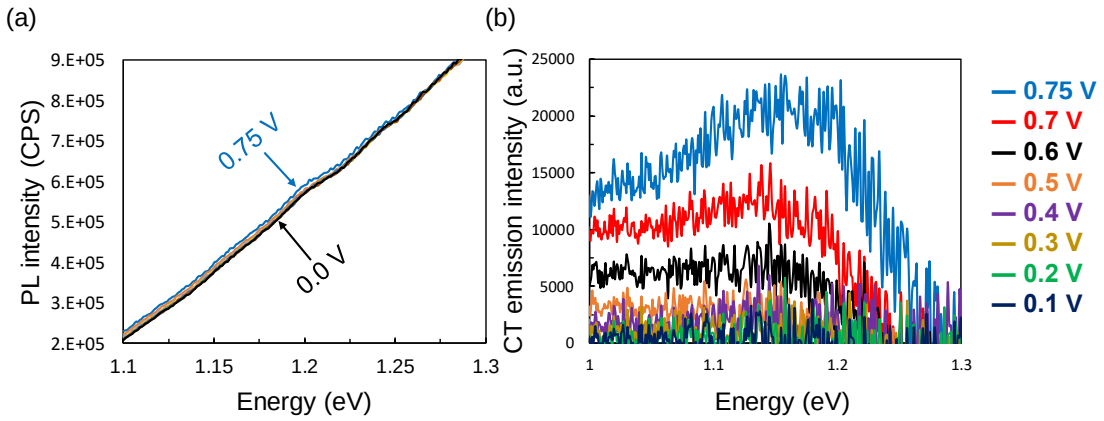

Figure 3.4.2. (a) PL spectra of the PTB7/PCBM device irradiated by 470 nm monochromatic LED under different applied voltages. (b) CT emission of PTB7/PCBM device under monochromatic light (470 nm) irradiation.

3.4.3 PL-*V* characteristics

The intensity of the CT state emission irradiated by 470 nm LED under applied voltage, was plotted with the photocurrent density flowing on the device during the PL measurement in **Figure 3.4.3**. Author got the two plots: voltage dependence of photocurrent density (*J*-*V* plot), and the voltage dependence of the PL intensity from the CT state recombination, call as PL-*V* plot. The *J*-*V* plot was the most important information for evaluating OSC performance but includes all the recombination events such as radiative and non-radiative recombination. Free charges become photocurrent or recombine. When the bias voltage is applied and photocurrent density (J) decreases, recombination current density (J_{rec}) increases accordingly. J_{rec} includes both radiative recombination current density (J_{rad}) and non-radiative recombination current density (J_{non}). PL-*V* plot corresponds to the normalized J_{rad} curve, because the PL-*V* plot includes the information only from the radiative recombination of the CT state.

The two plots present the opposite voltage dependence, namely: the photocurrent density increases from zero as the applied voltage decreases from V_{OC}, whereas The PL intensity decrease from V_{OC}. When the zero intensity of PL-*V* plot at 0 V is adjusted to J_{SC} of *J*-*V* plot, and the maximum intensity of PL at V_{OC} is adjusted to zero, the author can compare the voltage dependence of the photocurrent and the intensity of the recombination emission, i.e., FF of these two plots. **Figure 3.4.3** exhibited that there was a clear difference in the voltage dependence of the two plots: *J* gradually increased with the voltage decrease from V_{OC} to 0 V, whereas PL suddenly quenched from V_{OC} to 0.6 V. The *J*-*V* and PL-*V* plots are fitted by an equivalent circuit model of the diode [12], and the FF of the two plots were calculated as 49.81% and 71.73% in *J*-*V* and PL-*V*, respectively. FFs of J_{non} and photocurrent are the same, because the non-radiative recombination dominates the recombination process. However, in order to know the ideal *J*-*V* characteristics of the device, the voltage dependence of J_{rec} with completely eliminated J_{non} have to be measured. Because, non-radiative recombination path can be avoided in principle and radiative recombination is a thermodynamically inevitable loss process [6]. Thus, to measure the voltage dependence of CT state emission that is normalized J_{rad}-*V* characteristics can predict the ideal FF of the device, and provide new insights into the relationship between recombination mechanism and FF. The result indicated that additional recombination that the PL-*V* plot cannot detect take place when the OSC device was operated.

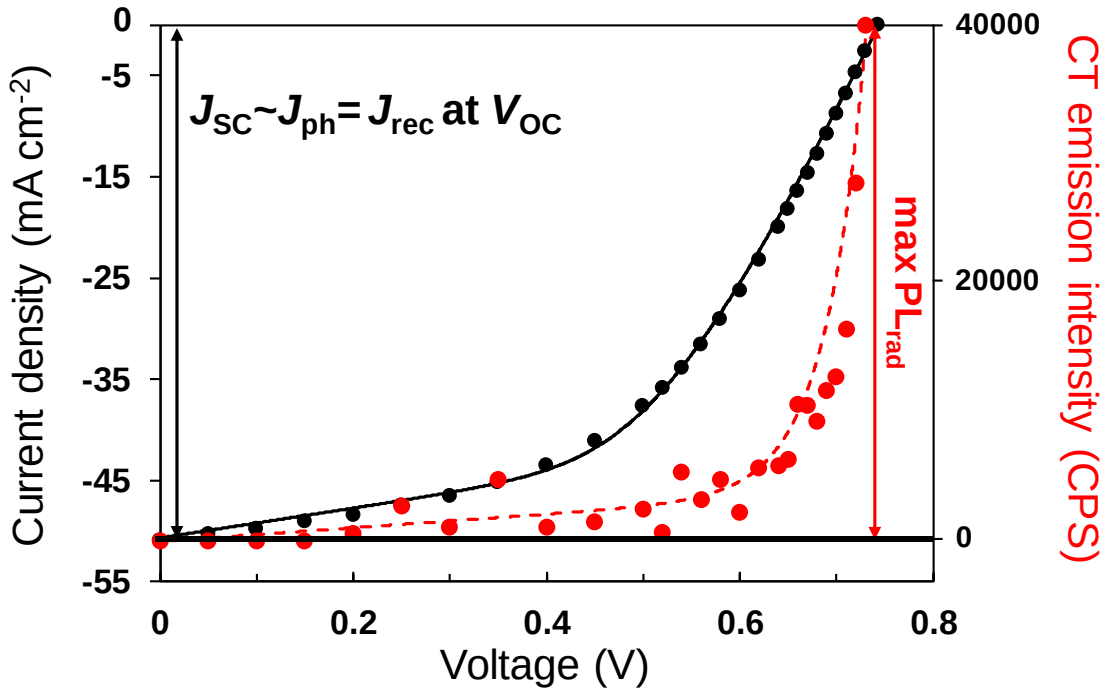

Figure 3.4.3. *J-V* and PL-*V* plots with the approximate curves of the PTB7/PCBM device under 470 nm monochromatic LED light irradiation.

3.4.4 Light intensity dependence of PL-*V* plot

To understand the origin of the FF difference between the *J*-*V* and the PL-*V* plots, the author investigated the light intensity dependence of those plots. The light intensity of 470 nm LED monochromatic light was fixed as 468 mW/cm^2 that was the same condition as **Figure 3.4.2** and **3.4.3**, the irradiated light intensity to the device was controlled by neutral density filters from 100% to 10%. The photocurrent density and the PL intensity were measured at the different applied voltages and plotted in **Figure 3.4.4 (a)** and **(b)**. The maximum PL intensity was normalized to the J_{SC} at each light intensity to compare the difference between the two plots. The FF of all the fitting curves was calculated and plotted in **Figure 3.4.4 (c)**. The FF of the *J*-*V* plots monotonically decreased from 66.73% to 49.81%, when the light intensity was increased from 10% to 100%, whereas FF of the PL-*V* plots kept constant over 70% regardless of the light intensity. The result indicated that the recombination that causes FF difference between the *J*-*V* and the PL-*V* plots were sensitive to the light intensity and promoted at high carrier concentration condition. Thus, to evaluate the FF difference of the two plots, the photocurrent density and the PL intensity values at the different applied voltages are plotted as a function of the light intensity. The plots were fitted by power functions and the slope values (α_{JV}, α_{PL}) were summarized in **Table 3.4.1**. The slope is 1; when the photocurrent and the PL intensity have a linear relationship with light intensity, but it decreases less than 1 when the recombination is promoted as a high carrier concentration condition. α_{PL}s kept the value close to 1 regardless of the applied voltage, whereas α_{JV} monotonically decreased as the applied voltage approaching the V_{OC} [13]. Thus, this indicates that the recombination that can be observed in the *J*-*V* plot has a large influence at high carrier concentration and smaller internal electric field close to the V_{OC}.

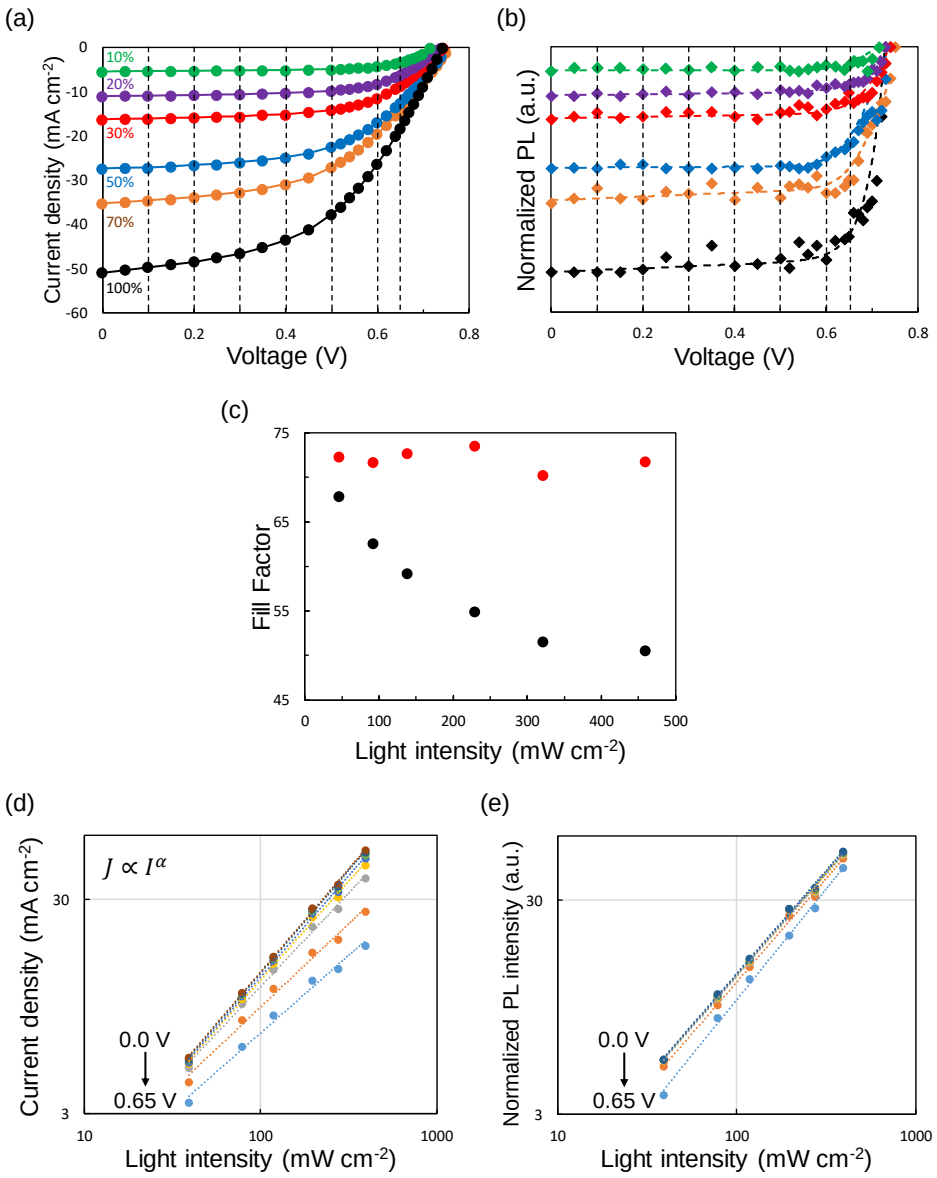

Figure 3.4.4. Light intensity dependence of (a) *J*-*V* and (b) PL-*V* plots with an approximate curve of the PTB7/PCBM device. (c) Fill Factor of the approximate curve of *J*-*V* (black) and PL-*V* (red) plots. The photocurrent density and the normalized PL intensity at the different applied voltage as a function of the light intensity. Light intensity dependence of JSC (d) and

normalized PL (e) with the bias voltage. The α is the slope of approximate line.

Injection voltage /V	α_{JV}	α_{PL}
0.1	0.9626	0.9627
0.2	0.9612	0.9585
0.3	0.9444	0.9565
0.4	0.9229	0.9548
0.5	0.8732	0.9565
0.6	0.7774	0.9675
0.65	0.7249	1.0345

Table 3.4.1. summary of the slope of *J*-*V* curve (α_{JV}) and PL-*V* plot (α_{PL}) with the injection voltage.

Figure 3.4.5 (a) and **(b)** are schematics of the different information detected by the *J-V* and PL-*V* plots, respectively. In the BHJ device, some photogenerated charges recombine such as radiative and non-radiative recombination before they reach the electrodes, and only extracted charges are reflected in the *J-V* plots. Non-radiative recombination includes not only recombination from CT state at D/A interface but also trap-assisted process, and occurs about a million times more often. In addition, the result of the light intensity dependence revealed that the recombination observed in the *J-V* plots is dominant at high carrier concentration and smaller in internal electric field conditions, indicating it occurs during charge transport [14]. In contrast, the PL-*V* plot is a method that directly observes the CT state recombination only at the D/A interface. Therefore, the main reason for bimolecular recombination during charge transport to electrode is non-radiative recombination process, and it is the essence that makes FF difference between *J-V* and PL-*V*. Thus, the PL-*V* plot predicts the ideal FF, which considers only the characteristics of charge separation and recombination near the D / A interface, is higher than that of the *J-V* plots.

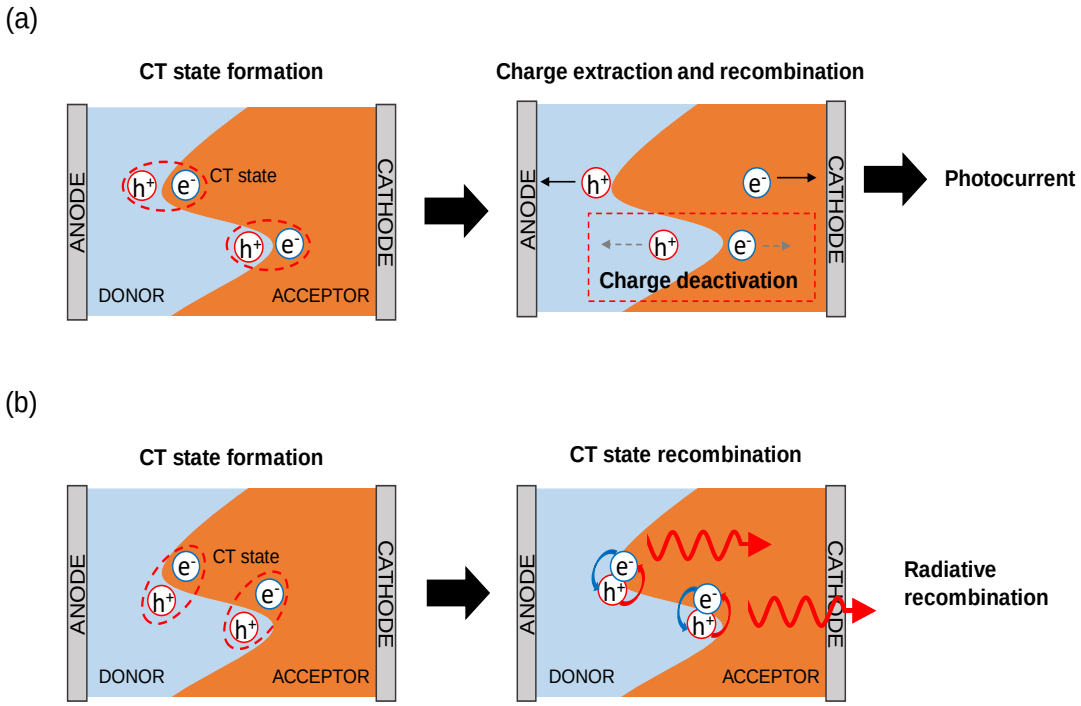

Figure 3.4.5. A simplified schematic of (a) the photoconversion process from CT state formation to charge extraction and (b) radiative recombination at D/A interface in as OSCs.

3.4.5 Activation energy of non-radiative recombination

The simultaneous measurement of photocurrent and recombination emission is a method for extracting the information of CT state emission at the interface. To investigate the origin of non-radiative recombination in OSCs, the CT state emission spectra extracted by subtracting PL spectra at short-circuiting from open-circuit excited by 470 nm LED in the PTB7/PCBM device, were observed under different temperature from 30 to -50°C in 5°C steps as shown in **Figure 3.4.6 (a)**. The intensity of CT state emission increases with decreasing device temperature. Thus, due to the non-radiative recombination induced by thermal vibration of the organic semiconductor molecules in the active layer was suppressed by cooling of the device temperature. The peak intensities of the CT state emission at various temperatures were plotted in **Figure 3.4.6 (b)**. The PL intensity from CT state is dominated by absorption, charge separation and emission efficiency. **Figure 3.4.7** shows the temperature dependence of *J*-*V* curves that were measured under simulated solar illumination (AM 1.5, 100 mW cm^{-2}) from a solar simulator. The result presents that J_{SC} is constant and indicates charge separation efficiency is temperature independence. The absorbance is also regarded as temperature independent. Therefore, it can be assumed that the CT state generation efficiency was constant under low temperature.

The temperature dependence of the PL intensity is expressed as the following thermal quenching formula because non-radiative recombination rates are thermally activated [15,16]:

$$I = I_0/[1 + a\exp\left(-\frac{E_a}{kT}\right)] \quad \text{equation 3.4.8}$$

where I is PL intensity, I_0 is the PL intensity at T = 0 K, a is the pre-exponential factor, k is Boltzmann constant, T is temperature and E_a is the thermal activation energy for inducing non-radiative recombination. The calculated E_a from the Arrhenius plot in **Figure 3.4.6 (b)** is 64.9 meV. The intramolecular vibration energy of rubrene that is typical donor molecules in an organic semiconductor has been reported as ~140 meV [17]. However, the energy of several intermolecular vibrational modes in a DNTT crystal that is a famous hole transporting material with high mobility has been reported as ranging from 2 and 12 meV [18]. Our result of the excitation energy for thermal activation of non-radiative recombination from the CT state was between the energy values of inter-and intra-molecular vibrations of organic semiconductors in the previous reports. This is possible because the molecular vibration of both donor and acceptor materials contributed to the intermolecular vibration of the CT state.

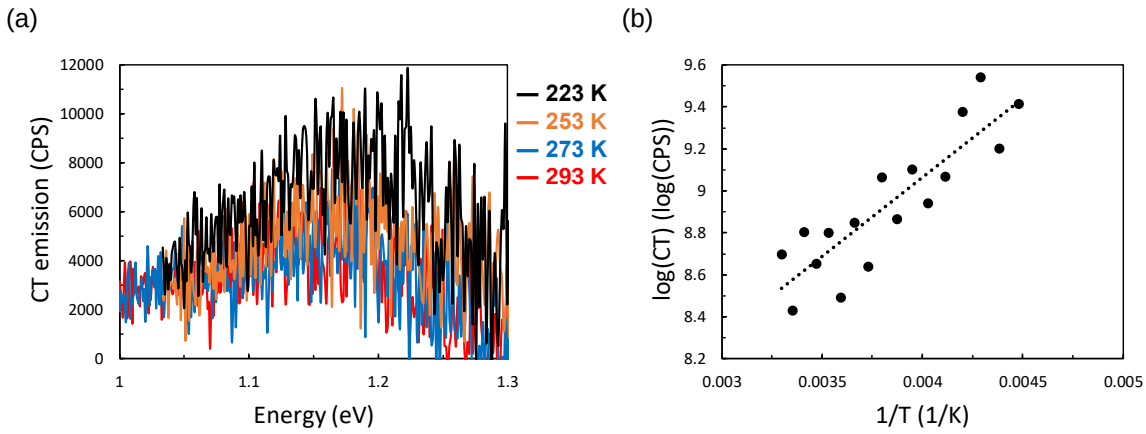

Figure 3.4.6. Temperature dependence of (a) CT emission spectra and (b) CT emission intensity of PTB7/PCBM device.

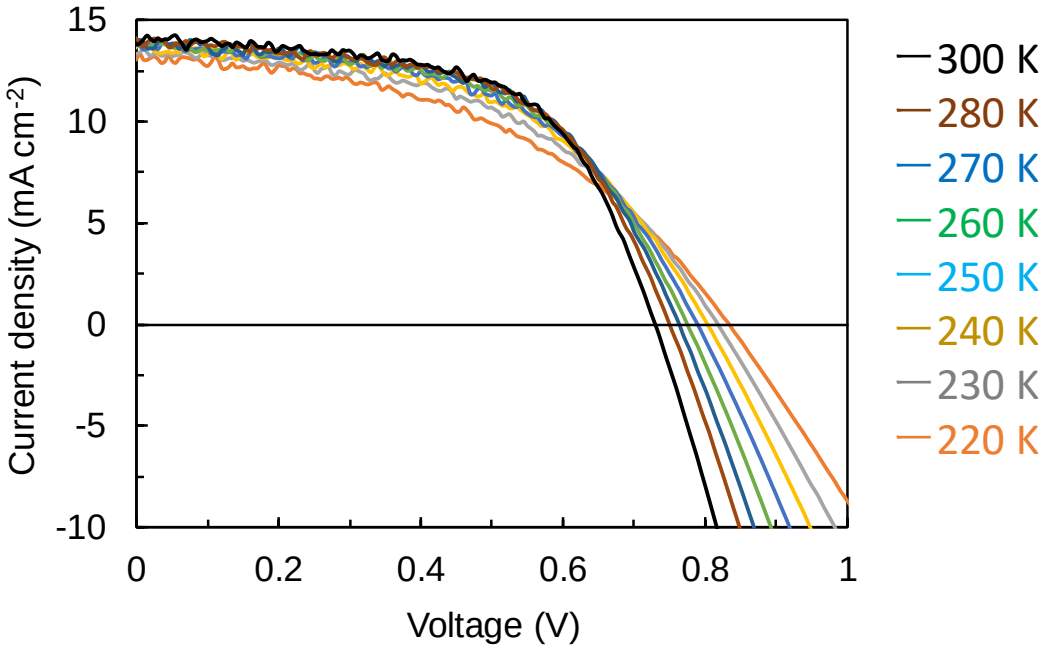

Figure 3.4.7. *J-V* curves for PTB7:PCBM BHJ device at various temperatures under AM 1.5 irradiation (100 mW cm^{-2}).

3.5 Conclusion

The author demonstrated the concept `PL-*V* plot` that includes the information only from the radiative recombination in the PTB7/PCBM device is one of the most famous D/A combinations in OSCs. The PL-*V* plots are different from *I*-*V* plots in voltage dependence, resulting in the FFs of *J*-*V* and PL-*V* plots were calculated as 49.81% and 71.73%, respectively. The light intensity dependence measurement revealed that the difference of FFs was due to the recombination during charge transport, and the PL-*V* plot predicts the ideal FF, which considers only the characteristics of charge separation and recombination near the D/A interface. Furthermore, the value of the activation energy for the non-radiative recombination is estimated by the temperature dependence of the CT state emission intensity. Our result demonstrated that the simultaneous measurement of photocurrent and recombination emission proposed in this study could be a strong tool for evaluating photoconversion characteristics at the D/A interface in OSCs.

3.6 References

[1] Y. Lin, M.I. Nugraha, Y. Firdaus, A.D. Scaccabarozzi, F. Aniés, A.H. Emwas, E. Yengel, X. Zheng, J. Liu, W. Wahyudi, E. Yarali, H. Faber, O.M. Bakr, L. Tsetseris, M. Heeney, T.D. Anthopoulos, A Simple n-Dopant Derived from Diquat Boosts the Efficiency of Organic Solar Cells to 18.3%, ACS Energy Lett. 5 (2020) 3663–3671. doi:10.1021/acsenergylett.0c01949.

[2] L. Zhan, S. Li, X. Xia, Y. Li, X. Lu, L. Zuo, M. Shi, H. Chen, Layer-by-Layer Processed Ternary Organic Photovoltaics with Efficiency over 18%, Adv. Mater. 33 (2021) 1–9. doi:10.1002/adma.202007231.

[3] K. Vandewal, S. Himmelberger, A. Salleo, Structural factors that affect the performance of organic bulk heterojunction solar cells, Macromolecules. 46 (2013) 6379–6387. doi:10.1021/ma400924b.

[4] S.M. Menke, N.A. Ran, G.C. Bazan, R.H. Friend, Understanding Energy Loss in Organic Solar Cells: Toward a New Efficiency Regime, Joule. 2 (2018) 25–35. doi:10.1016/j.joule.2017.09.020.

[5] J. Benduhn, K. Tvingstedt, F. Piersimoni, S. Ullbrich, Y. Fan, M. Tropiano, K.A. McGarry, O. Zeika, M.K. Riede, C.J. Douglas, S. Barlow, S.R. Marder, D. Neher, D. Spoltore, K. Vandewal, Intrinsic non-radiative voltage losses in fullerene-based organic solar cells, Nat. Energy. 2 (2017). doi:10.1038/nenergy.2017.53.

[6] K. Vandewal, K. Tvingstedt, A. Gadisa, O. Inganäs, J. V. Manca, Relating the open-circuit voltage to interface molecular properties of donor:acceptor bulk heterojunction solar cells, Phys. Rev. B - Condens. Matter Mater. Phys. 81 (2010) 1–8. doi:10.1103/PhysRevB.81.125204.

[7] N.K. Elumalai, A. Uddin, Open circuit voltage of organic solar cells: An in-depth review, Energy Environ. Sci. 9 (2016) 391–410. doi:10.1039/c5ee02871j.

[8] S. Foster, F. Deledalle, A. Mitani, T. Kimura, K.B. Kim, T. Okachi, T. Kirchartz, J. Oguma, K. Miyake, J.R. Durrant, S. Doi, J. Nelson, Electron collection as a limit to polymer:PCBM solar cell efficiency: Effect of blend microstructure on carrier mobility and device performance in PTB7:PCBM, Adv. Energy Mater. 4 (2014) 1–12. doi:10.1002/aenm.201400311.

[9] H. Kraus, M.C. Heiber, S. Väth, J. Kern, C. Deibel, A. Sperlich, V. Dyakonov, Analysis of Triplet Exciton Loss Pathways in PTB7:PC 71 BM Bulk Heterojunction Solar Cells, Sci. Rep. 6 (2016) 1–8. doi:10.1038/srep29158.

[10] B. Ebenhoch, S.A.J. Thomson, K. Genevičius, G. Juška, I.D.W. Samuel, Charge carrier mobility of the organic photovoltaic materials PTB7 and PC71BM and its influence on device performance, Org. Electron. 22 (2015) 62–68. doi:10.1016/j.orgel.2015.03.013.

[11] Z. He, C. Zhong, S. Su, M. Xu, H. Wu, Y. Cao, Enhanced power-conversion efficiency in polymer solar cells using an inverted device structure, Nat. Photonics. 6 (2012) 591–595. doi:10.1038/nphoton.2012.190.

[12] B.P. Rand, D.P. Burk, S.R. Forrest, Offset energies at organic semiconductor heterojunctions and their influence on the open-circuit voltage of thin-film solar cells, Phys. Rev. B - Condens. Matter Mater. Phys. 75 (2007) 1–11. doi:10.1103/PhysRevB.75.115327.

[13] A.K.K. Kyaw, D.H. Wang, V. Gupta, W.L. Leong, L. Ke, G.C. Bazan, A.J. Heeger, Intensity Dependence of Current À Voltage Characteristics and Recombination in High-E ffi ciency, ACS Nano. (2013) 4569–4577.

[14] C.M. Proctor, S. Albrecht, M. Kuik, D. Neher, T.Q. Nguyen, Overcoming geminate recombination and enhancing extraction in solution-processed small molecule solar cells, Adv. Energy Mater. 4 (2014). doi:10.1002/aenm.201400230.

[15] M. Leroux, N. Grandjean, B. Beaumont, G. Nataf, F. Semond, J. Massies, P. Gibart, Temperature quenching of photoluminescence intensities in undoped and doped GaN, J. Appl. Phys. 86 (1999) 3721–3728. doi:10.1063/1.371242.

[16] F. Tang, Z. Su, H. Ye, Y. Zhu, J. Dai, S. Xu, Anomalous variable-temperature photoluminescence of CsPbBr3 perovskite quantum dots embedded into an organic solid, Nanoscale. 11 (2019) 20942–20948. doi:10.1039/c9nr07081h.

[17] F. Bussolotti, J. Yang, T. Yamaguchi, K. Yonezawa, K. Sato, M. Matsunami, K. Tanaka, Y. Nakayama, H. Ishii, N. Ueno, S. Kera, Hole-phonon coupling effect on the band dispersion of organic molecular semiconductors, Nat. Commun. 8 (2017). doi:10.1038/s41467-017-00241-z.

[18] G. Schweicher, G. D'Avino, M.T. Ruggiero, D.J. Harkin, K. Broch, D. Venkateshvaran, G. Liu, A. Richard, C. Ruzié, J. Armstrong, A.R. Kennedy, K. Shankland, K. Takimiya, Y.H. Geerts, J.A. Zeitler, S. Fratini, H. Sirringhaus, Chasing the "Killer" Phonon Mode for the Rational Design of Low-Disorder, High-Mobility Molecular Semiconductors, Adv. Mater. 31 (2019). doi:10.1002/adma.201902407.

Chapter 4: General conclusion

4.1 Summary of this thesis

This thesis can be summarized as follows.

1) Using an ambipolar molecule, an organic *pn*-homojunction solar cell was realized. As the doping concentration of *p*- and *n*-layer increased, the energy offset of *pn*-interface increased, and the current–voltage characteristics changed. First, a large energy offset between adjacent molecules accelerated the charge separation; therefore, the photocurrent was promoted. However, the HOMO–LUMO gap between adjacent molecules decreased and it affected voltage drop. This result indicates that the charge recombination in organic *pn*-homojunction solar cells occurs from localized charge carriers at the adjacent molecules. The mechanism is compared with the CT state recombination in conventional D/A type OSCs, although the devices in this study were fabricated using a single host material and a doping technique resembling the inorganic *pn*-homojunction SCs.

2) As a method for directly measuring the recombination of the CT state, the author simultaneously measured the photocurrent and radiative recombination of the CT state under an electric field. CT state emission represents the maximum intensity in the open-circuit condition of the device. However, it quenches in the short-circuit conditions. The new concept, PL–*V* plot, contains only information about the radiative recombination and the FF is high from *I*-*V* characteristics. The result shows that

additional recombination that the PL-*V* plot cannot occur when the OSC device was operated. The light intensity dependence measurement revealed that the difference in FFs was attributed to recombination during charge transport. Moreover, the activation energy for the non-radiative recombination is estimated from the temperature dependence of the CT state emission intensity. For evaluating photoconversion characteristics, the simultaneous measurement of photocurrent and recombination emission could be a useful method.

4.2 Future prospects

To improve the efficiency of OSCs, the author proposes the following prospects above this study:

1) Although the organic *pn*-homojunction solar cell forms the idea of inorganic solar cells. As the result, its behavior is similar to that of a typical D/A type OSCs, because the charge carriers are localized to the molecules. However, organic *pn*-homojunction device do not affect the characteristics and is formed only by modifying the work function of host material. Therefore, if a band conductive organic semiconductor is used as the host molecule for fabricating the organic *pn*-homojunction solar cells, it will be possible to obtain the high V_{OC} and photoconversion efficiency. Recently, some organic semiconductors that show the band-like nature of charges are proposed. Thus, using these materials as hosts in organic *pn*-homojunction SCs could realize direct free charge formation and band-to-band recombination. The open-circuit voltage of the device will be determined by the bandgap of the materials. Finally, it will be possible to achieve a higher efficiency of organic *pn*-homojunction SCs, with enhanced photocurrent through doping.
2) Suppressing non-radiative recombination leads to voltage enhancement of the device. If the molecular vibration (or specific vibration mode) that directly affects the non-radiative recombination of the CT state can be suppressed, the voltage loss due to the non-radiative recombination can be reduced, and the photoelectric conversion efficiency can be improved. The thermal vibration of the CT state can be explored by measuring the temperature dependence of the PL-*V*.

List of Publications

1) Photoconversion Mechanism at the *pn*-Homojunction Interface in Single Organic Semiconductor.

Ji-Hyun Lee, Armand Perrot, Masahiro Hiramoto, Seiichiro Izawa

Materials, **13**, 1-8 (2020)

2) Simultaneous Measurement of Photocurrent and Recombination Emission in Organic Solar Cell

Ji-Hyun Lee, Masahiro Hiramoto, Seiichiro Izawa

Submitted

ChemRxiv, DOI: 10.33774/chemrxiv-2021-xz8mp

List of Supplementary Publication

1) Organic *pn* homojunction solar cell

Seiichiro Izawa, Armand Perrot, **Ji-Hyun Lee**, Masahiro Hiramoto

Org. Electron., **71**, 45-49 (2019)

2) Influence of *N*-Substituents on Photovoltaic Properties of Singly Bay-Linked Dimeric Perylene Diimides

Seiichiro Izawa, Kentaro Uchida, Mayuko Nakamura, Keisuke Fujimoto, Jérémy Roudin, **Ji-Hyun Lee**, Toshiyasu Inuzuka, Kazutaka Sanada, Masami Sakamoto, Yasuo Nakayama, Masahiro Hiramoto, and Masaki Takahashi

Submitted

Oral presentations in International Conferences

1) Photoconversion Mechanism at the *pn*-Homojunction Interface in Single Organic Semiconductor

Ji-Hyun Lee, Armand Perrot, Masahiro Hiramoto, Seiichiro Izawa

2020 International Conference on Solid State Devices and Materials, 28th September 2020

Poster presentations in International Conferences

1) Origin of Photocurrent Generation in Organic *pn*-Homojuction Solar Cells

Ji-Hyun Lee, Seiichiro Izawa, and Masahiro Hiramoto

10th International Conference on Molecular Electronics & BioElectronis

Nara Kasugano International Forum IRAKA, Nara, 25th June 2019

2) Photoconversion Mechanism in Organic *pn*-Homojuction Solar Cell

Ji-Hyun Lee, Seiichiro Izawa, and Masahiro Hiramoto

CEMS International Symposium on Supramolecular Chemistry and Functional Materials 2019,

Ito Hall, The University of Tokyo, Tokyo, 10th December 2019.

Oral presentations in Conferences (in Japanese)

1) Elucidating Photoconversion Mechanism in Organic *pn* Homojunction Solar Cells

Ji-Hyun Lee, Armand Perrot, Masahiro Hiramoto, Seiichiro Izawa

The 80th Japan Society of Applied Physics Autumn meeting,

Sapporo Campus, Hokkaido University, 21th September 2019.

Poster presentations in Conferences (in Japanese)

1) Material Investigation for Efficient Organic *pn* Homojunction Solar Cell

Ji-Hyun Lee, Seiichiro Izawa, Masahiro Hiramoto

The 66th Japan Society of Applied Physics Spring meeting,

Tokyo Institute of Technology, Tokyo, 10th March 2019.

2) In-situ Measurement of Radiative Recombination in Organic Solar Cell

Ji-Hyun Lee, Seiichiro Izawa, Masahiro Hiramoto

The 68th Japan Society of Applied Physics Spring meeting,

Online Virtual Meeting, 17th March 2021

Acknowledgement

I deeply appreciate Professor Masahiro Hiramoto at the Institute for Molecular Science, National Institute of Nature Science for providing me with the opportunity to study in his laboratory. I learned a lot of things from his passionate leading, discussion, and advice. I was always encouraged by his teachings.

I also greatly grateful to Dr. Seiichiro Izawa for his research guidance and professional discussion. His accurate and appropriate comments have supported my studies.

I would like to express my sincere gratitude to Prof. Satoshi Kera, Dr. Tetsuro Kusamoro, Dr.Toshikazu Nakamura of IMS, and Prof. Yasuo Nakayama of Tokyo University of Science for their reviews of this thesis.

I am thankful to the co-authors of the papers, Mr. Armand Perrot. I also thankful to all the group members Ms. Jaseela Palassery Ithikkal, Ms. Shoko Uto, and Ms. Yuka Nakamura all encouraged me with helpful advice.

I would like to thanks Mr. Tadashi Ueda at the IMS of the instrument center for experimental discussion and support.

Financial support from The Okazaki Shinkin Bank and Japan Society for the Promotion of Science is gratefully acknowledged.

Finally, I deeply appreciate my family for encouraging and supporting me.